2010-08-10

Temperature and Variability of Three Ionian Volcanoes

Daniel R. Allen
Brigham Young University - Provo

Temperature and Variability of Three Ionian Volcanoes

Daniel R. Allen

A thesis submitted to the faculty of
Brigham Young University
in partial fulfillment of the requirements for the degree of

Master of Science

Denise C. Stephens, Advisor
Jani Radebaugh
Clark G. Christensen

Department of Physics and Astronomy

Brigham Young University

December 2010

ABSTRACT

Temperature and Variability of Three Ionian Volcanoes

Daniel R. Allen

Department of Physics and Astronomy

Master of Science

Cassini spacecraft images of Io obtained during its flyby of Jupiter in late 2000 and early 2001 were used to determine the lava composition and eruption style of three faint hotspots, Pillan, Wayland, and Loki. We found a maximum color temperature of 1130±289 K for Pillan and maximum color temperatures of 1297±289 K and 1387±287 K for Wayland and Loki, respectively. These temperatures are suggestive of basaltic lava. The temperatures with the best signal-to-noise ratios also suggested basaltic lava and were found to be 780±189 K, 1116±250 K, and 1017±177 K for Pillan, Wayland, and Loki, respectively. Pillan showed increased activity on the third eclipse day after being fairly constant for the first two days, suggesting increased fountaining or lava flow activity on the third day. The data also suggest that Pillan is surrounded by topography that blocked emission on day000 and caused a much more dramatic decrease in emission. Wayland's intensity decreased over the three eclipses, consistent with a cooling lava flow or decreasing eruption. However, rapid decreases in intensity over periods of 26 to 48 minutes could have resulted from the eruption of highly exposed lava, perhaps an open channel or fountain. The data also suggest Wayland may be in a depression surrounded by ridges that blocked part of the emission. Intensities at Loki over the course of the observation varied in both directions, and were consistent with previous determinations of an often quiescent lava lake with periods of active overturning and fountains.

ACKNOWLEDGMENTS

I would like to thank my committee for all of their help during the entire process from the analysis to the calculations to the writing. Their guidance and suggestions taught me many things and greatly improved not only the final product, but also my research and writing skills. I want to thank Dr. Jani Radebaugh for the idea of what to study and for her guidance on volcanoes and Io. It was a topic I knew very little about before this project but have grown to love. A huge thanks goes to Dr. Denise Stephens for making me work hard and greatly improving my thesis. Her help with the final image and error analysis was indispensable. I also want to thank Dr. Clark Christensen for serving as my committee chair during most of my thesis research. He was always available for signatures and filling out forms. I also couldn't have done this without Dr. Ben Taylor's help with the statistics and errors. Finally, I want to thank my family who supported me and stood by me when it felt like I would never be finished. Kathleen was my biggest cheerleader and kept me going. Symphany's smiling face when I came home after a long day at school made it all worthwhile.

Contents

List of Tables

List of Figures

Chapter 1

Introduction and Background

1.1 Motivation

A study of the surface of Jupiter's volcanically active moon, Io, provides insight into what the surface of the Earth and other planets may have been like billions of years ago. The primordial Earth was a much hotter, more violent world than the one we see today (Matson et al., 1998; Vlaar et al., 1994). The surface was covered with active volcanoes whose distribution and activity slowly waned as the Earth cooled (Vlaar et al., 1994). Other planets in the solar system were similarly active in the past (Christiansen and Hamblin, 1995). Today, only Io shows the same level of volcanic activity that must have existed on the primordial Earth and other planets. We can study Io to get a better understanding of what types of volcanic activity may have existed on the surface of the early Earth.

Studying Io also provides insight into the dissipation of heat as it relates to other tidally heated bodies. Because of its small size, Io should have cooled long ago, but tidal friction from Io's gravitational interaction with Jupiter and the other Galilean moons (Peale et al., 1979) produces heat that keeps the interior molten. The energy produced by tidal friction escapes to the surface through volcanic activity. Studying the distribution and nature of

Io's hotspots provides clues about its interior structure and how heat is being dissipated (Lopes-Gautier et al., 1999; Lopes et al., 2004). It also provides estimates of how much heat is being generated by tidal friction.

1.2 Io Volcanism and Tidal Heating

Io's volcanism comes from tidal heating. A planetary body undergoes tidal heating when it is subject to tidal stresses produced by the gravitational pull of another body or bodies. In the case of Io, its gravitational interaction with Jupiter and the other Galilean satellites results in a forced eccentricity of its orbit. (Peale et al., 1979). Because of this forced elliptical orbit, Io's distance from Jupiter changes as it revolves about the gas giant resulting in a change in the magnitude of the tidal force.

The change in tidal force causes Io's surface to rise and fall by up to 100 m from the differential stresses (Peale et al., 1979). By comparison, the tidal forces exerted on the Earth by the Sun and Moon are smaller by several orders of magnitude. The largest solid surface amplitude, caused by the principal lunar semi-diurnal tide (M_2) at Earth's equator, is only ~63 cm (Wahr, 1995). Earth's largest oceanic tides have an amplitude of only 18 m (Wood, 2003).

The frictional heat caused by tidal stresses melts the interior of Io and is dissipated through the formation of volcanoes and hotspots on the surface (Peale et al., 1979). By studying the temperature of the volcanoes and hotspots, we can estimate the energy output and thus the amount of energy produced in the interior through tidal friction (Lopes-Gautier et al., 1999). We can also model the composition of the moon's interior by inferring the composition of the volcanoes and hotspots from their measured temperatures (Keszthelyi and McEwen, 1997; Lopes-Gautier et al., 1999).

Lavas of different composition emit radiation and are liquid at different characteristic

temperatures. For example, silicates are common in the solar system and melt at different temperatures consistent with their composition. Basaltic lavas are silicate lavas that are rich in iron and magnesium, but ultramafic lavas are silicate lavas with increased magnesium content. Since magnesium has a higher melting temperature than iron, silicate rock richer in magnesium has a higher melting point. We can identify these different types of lavas on Earth and measure the temperatures at which they emit using on-site and remote sensing methods (Francis and Rothery, 1987; Oppenheimer and Rothery, 1991; Rothery et al., 1988; Wilson and Head, 1983).

Assuming that all the rocky planets and moons have similar compositions, scientists can measure the temperature of lava on another planet and infer the composition of the lava from measurements of lava on Earth (Christiansen and Hamblin, 1995; Grossman, 1972). The validity of applying these values to temperatures of other bodies in the solar system through the use of satellites and remote sensing has been demonstrated by Rothery et al. (1988), Francis and Rothery (1987) and Oppenheimer and Rothery (1991). This forms the basis for comparing lavas on Earth and Io and determining their compositions.

Io shows several examples of the two main types of volcanic eruptions, explosive and effusive. Volcanic plumes made of S_2 (Spencer et al., 2000) and SO_2 (Pearl et al., 1979) are one form of explosive eruption. Most hotspots show evidence of this explosive type in the form of active plumes or plume deposits that ring the volcano (see Fig. 1.1). Because of Io's low gravity and minimal atmosphere, the plumes rise to heights of hundreds of kilometers above the surface and fall back to form large colorful rings (Davies, 2007; Kieffer, 1982; Wilson and Head, 1983, 2001, 2003). The color comes from the sulfur and various impurities (Geissler et al., 1999; Kargel et al., 1999). Mafic pyroclastic eruptions are another type of explosive eruption that form dark diffuse deposits around volcanic centers as seen in Figure 1.1b (Williams et al., 2002).

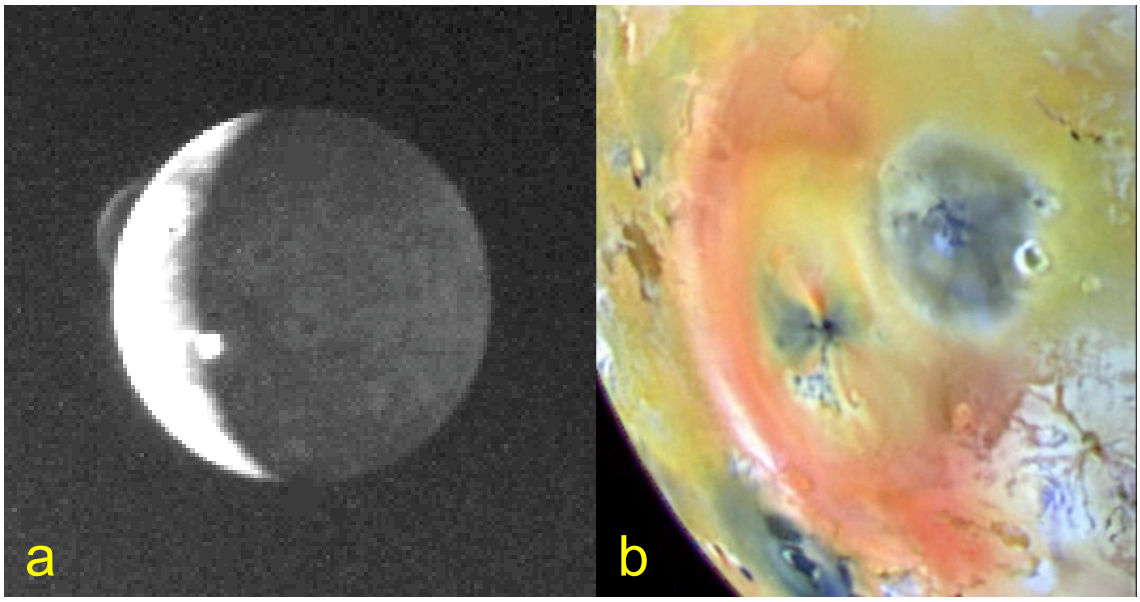

Figure 1.1 ***Left(a)****: The original plume discovery image from 1979 showing a 260 km high plume above Pele on the left and a plume above Loki at the terminator.* ***Right(b)****: False-color Galileo image showing Pele with a bright red plume deposit and Pillan with a dark plume deposit after an eruption in 1997 (NASA JPL Photojournal website; Davies, 2007).*

The effusive eruption type can be subdivided into three broad styles: Promethean, Pillanian, and Lokian (Lopes and Williams, 2005). They often occur near volcanic features called paterae. Paterae are depressions similar to terrestrial calderas that are thought to form by collapse over shallow magma chambers (Radebaugh et al., 2001) (Fig. 1.2). The three types of effusive eruptions are described below.

- Promethean eruptions are characterized by extensive compound lava flow fields produced by repeated breakouts of basaltic lava (Keszthelyi et al., 2001). This is similar to the slowly emplaced lava fields at Kilauea in Hawaii. They are generally long-lived eruptions lasting years at a time and can include small (< 200 km high) sulfurous plumes (Lopes and Williams, 2005). Temperatures and emission are generally lower

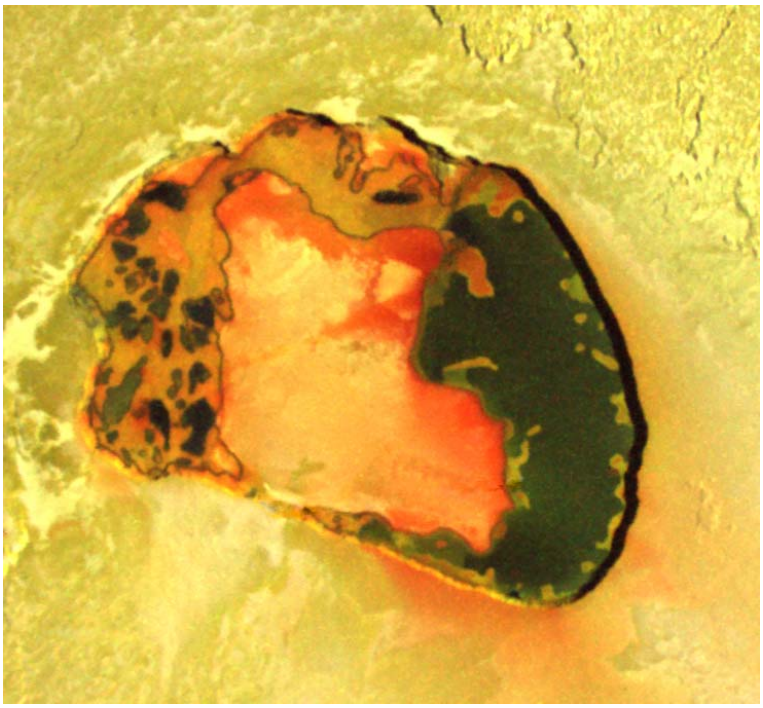

Figure 1.2 *False-color Galileo image of Tupan patera (NASA JPL Photojournal website). Light from the right side of the image illuminates the left side of the depression and casts shadows over the right side. The colors come from sulfur and impurities (Geissler et al., 1999; Kargel et al., 1999).*

than for the other two types and are decreasing. The temperatures are characteristic of insulated, cooling lava, but they can be higher if a breakout event occurs.

- Pillanian eruptions have short lifetimes but release a large volume of material (Keszthelyi et al., 2001). They produce large lava flows over a period of months and large (> 200 km high), explosive plumes (Lopes and Williams, 2005). The temperatures range from basaltic, 1300 K - 1550 K lava with low viscosity and varying amounts of iron and magnesium, to ultramafic, 1700 K - 1900 K lava rich in magnesium with low viscosity (McEwen et al., 1998b). Temperatures and emission vary depending on the conditions

present. The Galileo spacecraft observed the defining event in 1997 as Pillan erupted 56 cubic kilometers of lava over an area of 5600 km^2 in a matter of months (Davies, 2006). By comparison, in 1980 Mount St. Helens erupted only 0.3 km^3 of lava (Casadevall et al., 1983).

- Lokian eruptions are confined within paterae and are associated with lava lakes (Lopes et al., 2004). Some show signs of overturning and lava fountains like Pele (Howell, 1997; Radebaugh et al., 2004; Rathbun et al., 2002). Fountains and overturning are associated with increases in temperature and emission. Plumes can also develop over these lava lakes (Morabito et al., 1979; Spencer et al., 2000).

Although there are three main styles of effusive eruption, many hotspot locations show evidence of more than one style of eruption occurring or having occurred. Pele produces Pillanian and Lokian styles and Tvashtar shows all three (Lopes and Williams, 2005). Most hotspots also exhibit explosive and effusive qualities in their activity (Lopes and Williams, 2005).

1.3 History of Observations

The types and styles of volcanism on Io are varied and so is its history of observations. Galileo first turned his telescope on the Jovian system in 1610 and discovered what would afterwards be named the Galilean satellites (Lopes and Williams, 2005). Io is one of these satellites. Observations continued over the centuries and began to increase in the 1960s when Binder and Cruikshank (1964) reported a brightening of Io as it emerged from eclipse. Witteborn et al. (1979) saw an intense, temporary brightening at 2 to 5 microns in the infrared and measured a surface temperature of 600 K.

Despite several observations to the contrary in the 1960s and the early 1970s (Morrison

et al., 1972; Witteborn et al., 1979), Io was thought to be a dead planet much like the Moon. The passage of Voyager 1 in 1979 overturned that theory by returning pictures of a young, colorful surface with volcanic plumes rising several hundred kilometers above the surface (Fig. 1.1). Researchers questioned whether the volcanism was sulfur or silicate in nature. Temperatures of a few hundred kelvin and spectral data indicating the presence of S_2 and SO_2 suggested sulfur volcanism, but the bulk density of $\sim$3500 kg m^{-3} and the presence of 9 km high mountains favored silicates (Carr, 1986; Fanale et al., 1979; Pearl et al., 1979; Wamsteker et al., 1974). Post-Voyager ground-based observations by Johnson et al. (1988) and Veeder et al. (1994) confirmed temperatures between 900 K and 1500 K for hotspots on the surface, too hot for sulfur volcanism.

Subsequent ground-based and Galileo spacecraft observations have led to the discovery of ultramafic lavas with temperatures in excess of 1600 K at a few hotspots, further supporting the view that volcanic activity on Io is silicate in nature (Davies et al., 2001; McEwen et al., 1998b; Spencer et al., 1997). Ultramafic lavas are similar to terrestrial komatiitic lavas that were widespread on the Earth billions of years ago (Davies, 2007; Williams et al., 2001a). Ultramafic lavas have a higher melting temperature because of their increased magnesium content relative to basaltic lava, which is more iron rich. Magnesium itself has a higher melting point than iron and thus requires higher temperatures and a higher degree of partial melt of the surrounding rocks in order to be incorporated into a lava.

Remote sensing has revealed many high temperature measurements for Ionian volcanoes. Spencer et al. (1997) found temperatures of at least 1500 K using the Infrared Telescope Facility on Mauna Kea at the same time that Davies (1997) and Lopes-Gautier et al. (1997) were reporting hotspots in excess of 1000 K using Galileo NIMS data. A temperature of 1470$\pm$20 K was recorded during an outburst of Surt by Marchis et al. (2002) using adaptive optics on the Keck II telescope. These temperatures indicate that the volcanism is primarily

silicate in nature. Although the volcanism is primarily silicate in nature, sulfur and sulfur dioxide are still observed to play a role in the formation of plumes and frost on the surface that may produce secondary lava flows (Williams et al., 2001b).

Recent data from Cassini and New Horizons also show temperatures consistent with basaltic and possibly ultramafic volcanism. Radebaugh et al. (2004) analyzed data from the Cassini spacecraft and found a temperature of 1500±80 K for Pele. They concluded that the lava was most likely basaltic, but they couldn't rule out ultramafic with temperatures right on the upper limit of basalt. Milazzo et al. (2005) found color temperatures of 1300 K at Tvashtar with the possibility of higher temperatures. Initial data from New Horizons indicates minimum magma temperatures of 1150 to 1335 K for the brightest hotspots on Io, which are consistent with basalt (Spencer et al., 2007).

Of particular interest to us is the observational history of the three hotspots central to this study: Pillan, Wayland, and Loki. Temperatures measured by the Galileo spacecraft for Pillan have been among the highest measured for any hotspot on Io. McEwen et al. (1998b) reported brightness temperatures of 1500-1800 K, and Davies et al. (2001) quoted a temperature of 1870 K during a 1997 outburst of Pillan. Later work by Keszthelyi et al. (2007) suggested that these temperatures should be lowered by ∼260 K after applying new models, placing the temperatures firmly within the basaltic regime.

Temperatures have not been reported for Wayland, but based on its observational history as a consistently emitting hotspot, we might expect the temperatures for this hotspot to also be basaltic in composition.

Loki has been studied extensively through ground-based observations and analysis of Galileo data. Typically, temperatures have been less than 1000 K and generally reside around 400-700 K (Davies, 2003; Howell and Lopes, 2007; McEwen et al., 1998a; Rathbun et al., 2002). However, Blaney et al. (1995) found a value of 1225 K from ground-based

observations of an outburst in January 1990. Davies (1996, 2003) also suggested that higher temperatures (1100 K-1470 K) for Loki are possible if emission from deep in the cracks on the surface of the lava is observed.

Observations and analyses of the volcanoes and hotspots on Io continue today through ground-based observations and the use of archived mission data. Equipped with adaptive optics, the Keck II telescope provides current observations and monitoring of Io's volcanic activity. For example, Rathbun and Spencer (2006) are continuing their observations of Loki, and Laver et al. (2007) determined a temperature of 1240±4 K in April 2006 for Tvashtar. Marchis et al. (2005) and de Pater et al. (2004) have also continued their observations of several hotspots using Keck. Current ground based observations and archived data from the Galileo, Cassini, and New Horizons missions provide continuing opportunities to perform detailed studies on Io's volcanic activity.

1.4 Cassini Spacecraft and Mission

Cassini was launched on October 15, 1997 to study Saturn and its satellites. On its way, it flew past the Jupiter system and obtained images of the surface of Io in late 2000 and early 2001 (Porco et al., 2003). Cassini collected nearly 500 images (Fig. 1.3) of Io over a wavelength range of 250-1050 nm while it was eclipsed by Jupiter (Porco et al., 2003). The 500 images were collected in three different datasets, during three different eclipses over a period of four days. Each dataset was collected over a period of two to three hours with individual images separated from each other by several seconds to a few minutes (Table 1.1). This resulted in the best temporal resolution to date of Io's hotspots seen from a spacecraft (Radebaugh et al., 2004). We report our analyses of these images for the brightest visible hotspots on Io and their implications for the interior and surface composition and temperature.

Day	SSC Lat	SSC Lon	Time of Obs.	Time between CL and IR	Time between CL
364	$\sim 0.5^o$ N	300^o-324^o W	3 h	48 s	12 min
000	$\sim 0.2^o$ S	286^o-302^o W	2 h	3 min 13 s	8 min 48 s
001/002	$\sim 0.8^o$ S	280^o-305^o W	3 h	48 s	12 min

Table 1.1 *Details of the Cassini eclipse observations of Io. SSC Lat and SSC Lon are the subspacecraft latitude and longitude. The last three columns indicate the total time of observation on each day as well as the time between successive images and successive image pairs.*

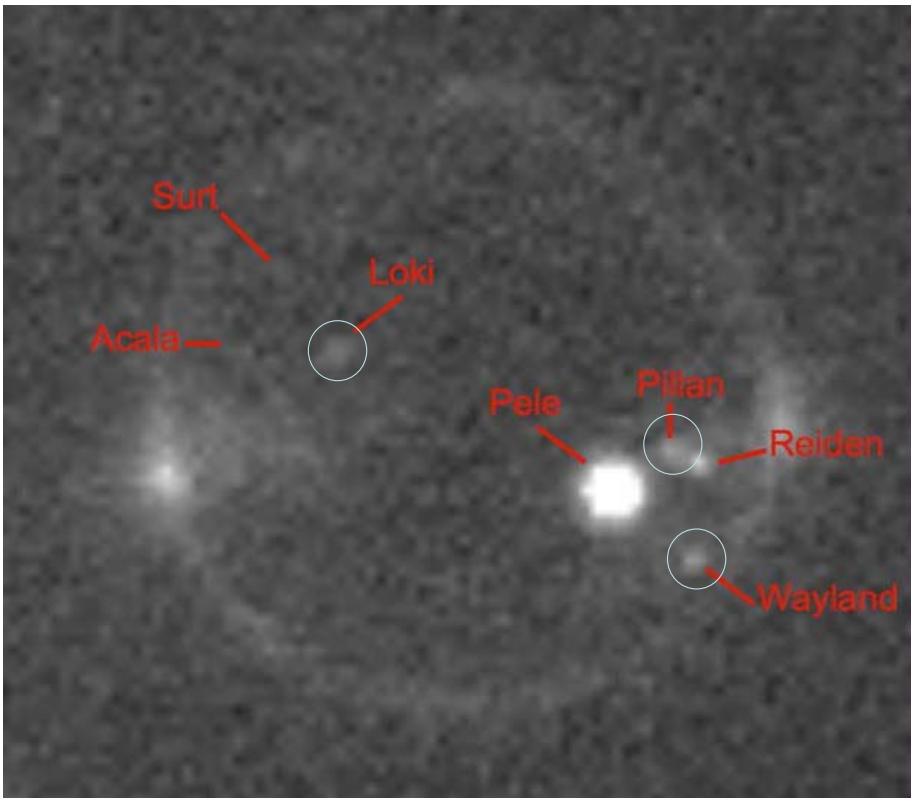

Figure 1.3 *Clear filter image of Io in eclipse by Jupiter showing the most prominent hotspots with the circles indicating the three in this study. The image was taken January 1, 2001 by Cassini ISS at a resolution of 61 km/pixel. The emission near Io's limb are auroral glows due to excitation of plume gases (Radebaugh et al., 2004).*

Chapter 2

Data and Reduction Procedures

2.1 Cassini and the Raw Data

Cassini was launched with an array of instruments aboard including the Imaging Science Subsystem (ISS) which contained the narrow-angle camera (NAC) used in this research. NAC is comprised of a 1024x1024 square CCD array with a focal length of 2000 mm and a 0.35^o field of view. In addition to taking high-resolution images of astronomical targets, NAC is used for optical navigation of the spacecraft. NAC has a double filter wheel system with 12 filters in each wheel. Each wheel contains 11 filters of varying wavelengths and a clear filter. When both clear filters are used, the detector is sensitive to light from 250 nm out to 1050 nm (Porco et al., 2004).

We used images of Io taken through the two clear (CL) filters and through one clear filter and the infrared 4 (IR) filter in our analysis because they gave the best signal-to-noise ratio for the hotspots (Fig. 1.3). The CL filter configuration has a wavelength range of 250 nm to 1050 nm while the IR configuration ranges from 875 nm to 1050 nm (Porco et al., 2004). NAC took ∼500 total images of Io at a distance of 9.72 million km, resulting in a resolution of ∼58 km/pixel (Porco et al., 2003). Many of the 500 images were taken through

different filters and did not contain at least one of our hotspots. Consequently, they were not used. Sixty-nine images taken through the CL and the IR filter configurations were found to contain at least one of our hotspots at a sufficient signal-to-noise ratio for our analysis (Tables 2.1 and 2.2).

We divided the 69 images into sequences according to which eclipse and day they were taken. The last two days of images were taken during the third eclipse. Each sequence of images ranged in time from 2-3 hours with exposure times between 2-12 seconds for each image depending on the day. As the NAC cycled through its filters, it captured a CL filter image or IR filter image every 12 minutes for eclipses 1 and 3 and every 8 minutes and 48 seconds for eclipse 2 (Table 1.1). Adjacent CL and IR images were spaced less than a minute apart for eclipses 1 and 3 and about 3 minutes apart for eclipse 2. This gave unprecedented temporal resolution for images taken by a spacecraft around Io, greatly improving the chance of correctly classifying the eruption style of the hotspots.

Better temporal resolution improves the chances of correctly classifying the eruption style of a hotspot because many volcanic processes are short-lived. For example, events such as lava fountains might not be seen with lower temporal resolution images, resulting in an incorrect classification. Observations at lower temporal resolution taken by the Galileo spacecraft, New Horizons, and ground-based telescopes have been used to study the temperature and variability of numerous hotspots on the surface (Davies et al., 2001; Howell and Lopes, 2007; McEwen et al., 1998a; Radebaugh et al., 2004; Spencer et al., 2007). Using techniques similar to these previous studies, we used the improved resolution Cassini data to look at the temperature and variability of three additional hotspots: Pillan, Wayland, and Loki (Fig. 1.3).

Date	UT Time	Image	Filter	Hotspot	Exp. Time (sec)
12/29/2000	09:13:50.321	n1356773129	CL	P, W	2
(Day 364)	09:14:38.321	n1356773177	IR	P, W	2
(Eclipse 1)	09:25:50.316	n1356773849	CL	P, W	2
	09:26:38.316	n1356773897	IR	P, W	2
	09:37:50.311	n1356774569	CL	P, W	2
	09:38:38.311	n1356774617	IR	P, W	2
	09:49:50.306	n1356775289	CL	P, W	2
	09:50:38.306	n1356775337	IR	P, W	2
	10:01:50.301	n1356776009	CL	P	2
	10:02:38.301	n1356776057	IR	P	2
	10:13:50.296	n1356776729	CL	P	2
	10:14:38.296	n1356776777	IR	P	2
	10:37:50.286	n1356778169	CL	P	2
	10:38:38.286	n1356778217	IR	P	2
12/31/2000	03:38:14.264	n1356925794	CL	P, W	2
(Day 000)	———	———	IR	P, W	3.2
(Eclipse 2)	03:47:02.261	n1356926322	CL	P, W	2
	03:43:49.062	n1356926130	IR	P, W	3.2
	03:55:50.257	n1356926850	CL	P, W	2
	03:52:37.058	n1356926658	IR	P, W	3.2
	04:04:38.253	n1356927378	CL	P, W	2
	04:01:25.055	n1356927186	IR	P, W	3.2
	04:13:26.250	n1356927906	CL	P, W	2
	04:10:13.051	n1356927714	IR	P, W	3.2
	———	———	CL	P	2
	04:19:01.047	n1356928242	IR	P	3.2
01/01/2001	22:12:50.203	n1357079071	CL	P, W	2
(Day 001)	22:13:38.202	n1357079119	IR	P, W	2
(Eclipse 3)	22:24:50.198	n1357079791	CL	P, W	2
	22:25:38.197	n1357079839	IR	P, W	2
	22:36:50.193	n1357080511	CL	P, W	2
	22:37:38.192	n1357080559	IR	P, W	2
	22:48:50.188	n1357081231	CL	P, W	2
	22:49:38.187	n1357081279	IR	P, W	2
	23:00:50.183	n1357081951	CL	P, W	2
	23:01:38.182	n1357081999	IR	P, W	2
	23:12:50.178	n1357082671	CL	P	2
	23:13:38.177	n1357082719	IR	P	2
	23:24:50.173	n1357083391	CL	P	2
	23:25:38.173	n1357083439	IR	P	2
	23:36:50.168	n1357084111	CL	P	2
	23:37:38.168	n1357084159	IR	P	2
01/02/2001	00:00:50.158	n1357085551	CL	P	2
(Day 002)	00:01:38.158	n1357085599	IR	P	2
(Eclipse 3)	00:12:50.153	n1357086271	CL	P	2
	00:13:38.153	n1357086319	IR	P	2

Table 2.1 *The images used in this study for Pillan and Wayland.* ***Note****: Pillan (P) and Wayland (W)*

Date	UT Time	Image	Filter	Hotspot	Exp. Time (sec)
12/29/2000	09:17:40.320	n1356773369	CL	L	12
(Day 364)	09:15:16.321	n1356773225	IR	L	12
(Eclipse 1)	09:29:40.315	n1356774089	CL	L	12
	09:27:16.316	n1356773945	IR	L	12
	09:41:40.310	n1356774809	CL	L	12
	09:39:16.311	n1356774665	IR	L	12
	09:53:40.305	n1356775529	CL	L	12
	09:51:16.306	n1356775385	IR	L	12
	10:05:40.300	n1356776249	CL	L	12
	———	———	IR	L	12
	10:17:40.295	n1356776969	CL	L	12
	10:15:16.296	n1356776825	IR	L	12
	10:29:40.290	n1356777689	CL	L	12
	10:27:16.291	n1356777545	IR	L	12
	10:41:40.285	n1356778409	CL	L	12
	10:39:16.286	n1356778265	IR	L	12
	10:53:40.280	n1356779129	CL	L	12
	10:51:16.281	n1356778985	IR	L	12
	11:05:40.275	n1356779849	CL	L	12
	11:03:16.276	n1356779705	IR	L	12
01/01/2001	22:16:40.201	n1357079311	CL	L	12
(Day 001)	22:14:16.202	n1357079167	IR	L	12
(Eclipse 3)	22:28:40.196	n1357080031	CL	L	12
	22:26:16.197	n1357079887	IR	L	12
	22:40:40.191	n1357080751	CL	L	12
	22:38:16.192	n1357080607	IR	L	12

Table 2.2 *The images used in this study for Loki (Loki (L))*

2.2 Data Reduction Procedures

The analysis began with the conversion of raw NAC images to files displayable in the Integrated Software for Imagers and Spectrometers (ISIS) and the Image Reduction and Analysis

Facility (IRAF). ISIS is a combination of programs designed to process and analyze remotely sensed data (ISIS website). Members of the Astrogeology team of the United States Geological Survey (USGS) originally wrote the program in 1971 and maintain the most recent version, ISIS 3. ISIS is used to process raw data from many of NASA's spacecraft missions.

IRAF is a similar combination of programs designed for the reduction and analysis of astronomical data. It is supported by the IRAF programming group at the National Optical Astronomy Observatories (NOAO) (IRAF Project Home Page). It is used most often for reduction and analysis of stellar objects from CCD images, but it can be used to process CCD images of hotspots since hotspots behave as point-spread functions (PSF) much like stars do.

The raw NAC images were downloaded from archived Cassini data at the NASA Planetary Data System website. Associated libraries and necessary help files needed for the image conversion were downloaded at the time ISIS was installed. We used the *vicar2isis* program to convert the raw image files into ISIS .cub files. We also used the *isis2fits* command to convert the .cub files into IRAF .fits files.

The initial data acquisition for each image required the use of both ISIS and IRAF. First, we displayed each .cub file using the *qview* program in ISIS. The *qview* program displays the image and provides a window with statistics about a chosen pixel. You can specify a box size around a given pixel and *qview* calculates the average pixel value or average data number (DN) in the box and the standard deviation of the pixel values in the box. More importantly, it provides the position of the given pixel in standard x-y format. We recorded the x-y positions of the hotspots in each image in separate coordinate files. The images were later processed using these coordinate files and IRAF to find the flux or signal from each hotspot.

The second step was to subtract the background contribution from each image. This

was done to facilitate finding the fluxes using IRAF, to remove a 'prime signal' or hum present in the images (Fig. 2.1), and to aid in the error calculations of the hotspot signal. The background subtraction required several steps for each image and involved creating an artificial background image with a separate background value for each row in the image.

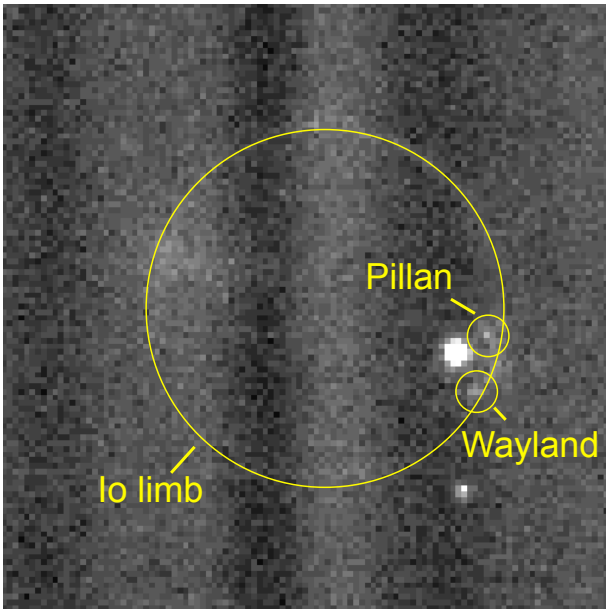

Figure 2.1 *Clear filter image showing Pillan, Wayland, and the limb of Io for day364. Care had to be taken during analysis as the hotspots neared the limb to avoid unwanted contributions from the auroral glows. Note the presence of a vertical prime signal or hum.*

First, we used the *gstatistics* program in IRAF to find the midpoint pixel value and standard deviation of all the pixels in the image. This gave us an idea of the overall background value in the image and allowed us to set upper and lower limits on the pixel values to accept in the next step (Fig. 2.2). We then examined the images and determined that a one σ or one standard deviation above and below the midpoint value was sufficient for the upper and lower cutoff values because the background pixels varied very little. Setting limits gave us better statistics for the background values in each row by removing bad pixels, like cosmic

```
                                  I R A F
                       Image Reduction and Analysis Facility
PACKAGE = imgtools
   TASK = gstatistics

images  = @gstat.n1357085791.txt  Images
(masks  =                       ) Masks
(groups =                      *) Range of groups
(g_accum=                     no) Accumulate over groups?
(fields =                  doall) Fields to be printed
(lower  =                  404.) Lower cutoff for pixel values
(upper  =                  448.) Upper cutoff for pixel values
(gstpar =                       ) Results of statistics on the last image (pset)
(mode   =                     al)
```

Figure 2.2 *Parameters used for the gstatistics program in IRAF. The upper and lower limits are set at 1σ above and below the midpoint pixel value for all the pixels in the image. This gives better statistics and removes contributions from bad pixels like those from cosmic rays.*

rays for example, before calculating the mean background value.

Next, we used *gstatistics* again to read out the background statistics for each row in the image to a file. We created a separate row statistics file for each image which contained the midpoint value and standard deviation along with other statistics about each row. The files produced for Pillan and Wayland included pixel values for columns 41-1023, while the images for Loki used pixel values for columns 41-511. The full rows were not used because they included some bad columns.

Third, we ran one computer program to read out the desired data from our row statistics files and another program to create a file used by IRAF to make the artificial background image (Fig. 2.3). The program *getval.pl* (Stephens, 2010a) reads an input row statistics file and writes out a specified value and its corresponding row number. In this case, we chose the midpoint value and wrote the values to a new file. We then input the new file into the *rep26t.f* (Stephens, 2010b) FORTRAN program which wrote out the midpoint values 1024 (512 for Loki) times for each row into an output file.

Finally, we used the background file created by *rep26t.f* and the IRAF program *rtextimage* to create a background image with every pixel in a given row in the image corresponding

Figure 2.3 *Typical background image created using the rtextimage program in IRAF. Each pixel in a given row corresponds to the midpoint value of that row found using the gstatistics program. The image is then used with the imarith routine in IRAF to subtract it from the image and remove the background.*

to the midpoint value found for that row (Fig. 2.3). This artificial background image was then subtracted from the corresponding original image using the *imarith* program in IRAF to produce a final image with the background removed. We repeated the background subtraction process for all of the images and then processed the final images with IRAF to determine the signal coming from the hotspots.

We continued the image analysis using the sky subtracted IRAF .fits files, the x-y coordinate files produced previously with ISIS, and the *phot* package in IRAF to find the signal from each hotspot in the images. The *phot* package contains several parameter files that must be set correctly in order to process the images. A complete discussion of the IRAF packages and parameters used in the analysis is found in Appendix C.

In IRAF, it is possible to specify a circular aperture around a given pixel and find the flux or signal in that aperture. The x-y coordinate files specify the position of the hotpots in each image and designate the pixel on which to center the aperture. We chose an aperture size of 1.5 pixels which resulted in an area of just over seven pixels that contributed to the signal. With a resolution of 58 km/pixel, most of the flux was contained within the central pixel. However, much like stars, the signal from the hotspots was spread out over more than one pixel. By looking at the images, we also determined that an aperture size of two was too big and included unwanted signal from nearby hotspots such as Pele and auroral glows from the limb of Io. We found the flux from the hotspots in all of the images in both the CL and IR filters and used these fluxes to find the color temperatures and errors.

2.3 Data Difficulties

The acquisition and analysis of our data was not without difficulties and the goals of the project had to be scaled back from the original plan. Originally, we planned to analyze all of the hotspots seen in Fig. 1.3 except for Pele which was previously done by Radebaugh et al. (2004). The problems arose due to low signal in the IR filter images (see Fig. 2.4). Surt and Acala were difficult to detect in the CL images and impossible to detect in the IR images. The signal-to-noise ratio wasn't sufficient enough to produce meaningful results using a color temperature analysis. Reiden was easier to see in the CL images but difficult to detect in the IR images as well.

The remaining hotspots, Pillan, Wayland, and Loki, were easily detectable in the CL images but were once again difficult to locate in the IR images. We used Pele, which was visible in all of the images, to locate the others. We counted the number of pixels left or right and up or down from the center of Pele to the center of a hotspot in the CL image. We then counted the same number of pixels left/right and up/down in the IR image to locate

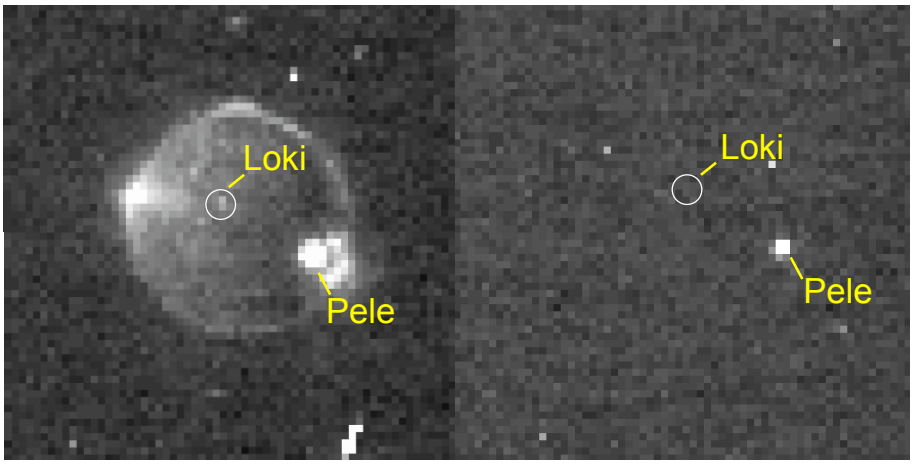

Figure 2.4 *Typical CL (left) and IR (right) images for Loki. The hotspot is typically only a few counts above background in the IR image. This leads to signal and error difficulties. (**Note**: Summation images were used for Loki, but regular images were used for Pillan and Wayland. Adjacent pixels were summed to increase the signal to noise ratio for the summation images (Geissler et al., 2004).)*

the hotspot. Since the images were taken relatively close together in time, we are confident that this method did a good job of locating the volcanoes. We also checked the neighboring pixels to the point found by this method, and they were lower in counts, indicating the IR signal was small but present.

With such a small IR signal, typically only a few counts above the background, interpretation of the temperatures was a delicate process. We found some temperatures that were unreliable because of low IR signal values. The CL signal was relatively constant for each hotspot, but the IR signal fluctuated. With a relatively constant CL signal, fluctuations in the IR signal greatly affected the final color temperatures. Random background fluctuations typical of CCD cameras affected the IR signal to a much greater extent because the signal was only a few counts above the background. When the background values were high, the

IR signal was very low resulting in an abnormally high temperature value. We considered a temperature reliable, if the IR signal-to-noise ratio (S/N) was greater than 1.5 (see Sec. 3.2). If the IR S/N was less than 1.5, then we removed the corresponding temperature and didn't consider it in our analysis. This added another degree of difficulty in interpreting the data.

Another possible source of difficulty and error was the NAC instrument and the data acquisition itself. The Cassini engineers designed the NAC to study the Saturnian system. Io and other planets imaged on the way to Saturn were not primary targets, but analyses of the data obtained still has value. The NAC instrument returned images with integers for the pixel values. While this is sufficient for bright objects, the low signal IR objects would have benefited from the extra fractions of flux lost or gained when truncating the values to integers. Finally, we were challenged by finding a ratio of two images considered to be simultaneous when in actuality they were acquired several seconds apart. Volcanic eruptions are dynamic over timescales of seconds. Changes to the surface may have occurred between the CL and IR images. The overall changes in emission and temperature must be considered carefully. Future missions capable of simultaneous observations in multiple filters should be able to address this.

Despite the data and instrument difficulties, we are confident that our efforts in regards to the low counts and our careful error analysis have given us meaningful results.

Chapter 3

Color Temperatures

3.1 Finding Color Temperatures

Color temperatures are found by taking observations in two different filters or wavelengths and comparing the ratio of the signals received by the NAC to the values obtained from the calibrated blackbody response curves of the NAC. The blackbody response curve from our two filters was found using the CL and IR filter transmission calibration files as discussed in Section 3.1.1.

Using color temperatures gave a better temperature estimate of the hotspot than single-filter derived brightness temperatures. This is because brightness temperatures average the flux over the entire pixel. With the low resolution of our images (58 km/pixel), the hotspots we image are much smaller than one pixel. A single pixel includes not only the hotspot, but also the low temperature area surrounding the hotspot. Thus, a brightness temperature underestimates the true temperature of the hotspot.

In contrast, color temperatures from ratios give one component of the temperature, the hotspot, found in a given pixel area with the low temperature background subtracted out. Calculating color temperatures using ratios from two filters is also simpler than finding

brightness temperatures because only the relative intensities at different wavelengths need to be measured. Many of the wavelength independent factors needed to calculate absolute radiances for brightness temperatures can be safely ignored (Radebaugh et al., 2004).

Color temperatures for Pillan, Wayland, and Loki were found by taking the ratio of the signal in the CL filter (250 nm - 1050 nm) to the IR filter (875 nm - 1050 nm) and comparing these values to the expected NAC blackbody response curve (Fig. 3.1). The two step process for finding the color temperatures is outlined in Sections 3.1.1 and 3.1.2. We first calculated the expected blackbody response curve. Then we plotted our signal ratios on the curve to determine the color temperatures.

3.1.1 Expected Blackbody Response Curve

We found the expected blackbody response curve for the NAC instrument using the system transmission calibration files for the CL filter and the IR filter. The transmission calibration files for each filter were produced by the Cassini ISS Team in collaboration with scientisits at JPL (Cassini ISS Imaging Science Team website) while NAC was still on the ground and during transit. Tests were run to understand and calibrate the camera's response and the percentage of light that would be detected as a function of wavelength for each filter. A transmission calibration file was then produced for each filter that listed the percentage of light transmitted as a function of wavelength.

We used the transmission calibration files to produce an expected blackbody response curve for our filters. First, we solved Planck's law (Eq. 3.1) as a function of wavelength over a range of temperatures from 200 K - 6400 K in increments of 100 K as follows:

$$I(\lambda) = \frac{2hc^2}{\lambda^5} \frac{1}{e^{\frac{hc}{\lambda kt}} - 1}. \tag{3.1}$$

For each temperature, we then calculated the total transmission, T_r, of the blackbody curve through each filter by convolving the fraction of light transmitted, F_t, from the transmission

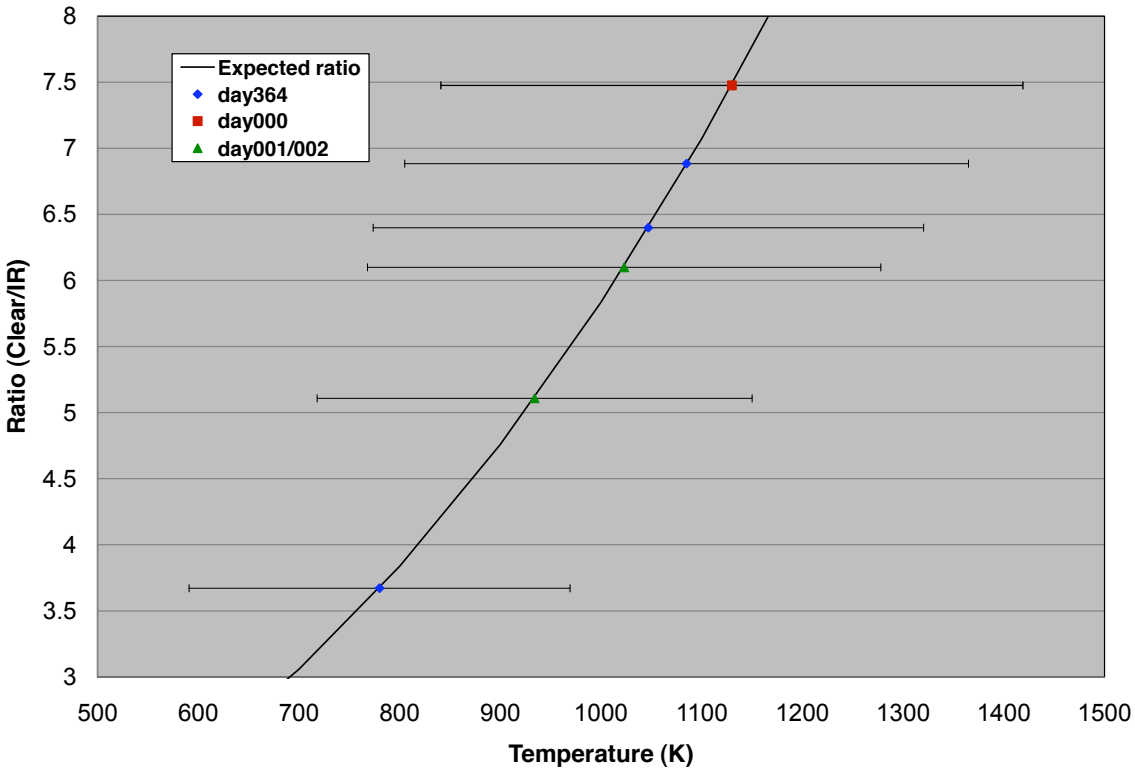

Figure 3.1 *Plot of ratios of emission from Pillan for CL and IR filters with the expected blackbody emission curve. The high color temperature is 1130±289 K and the low color temperature is 780±189 K. These temperatures suggest that the lava composition is most likely basaltic.*

calibration file with the Planck function $I(\lambda)$, over incremental steps in wavelength using:

$$T_r = \sum_i \lambda F_t I(\lambda). \tag{3.2}$$

where i represents each step in wavelength found in the transmission calibration file over the wavelength range of each filter. Finally, we took the ratio of the total transmission in the CL filter to the total transmission in the IR filter at each temperature increment and plotted the resulting expected blackbody response curve seen in Figure 3.1.

3.1.2 Signals and Ratios

The second step was plotting the signal ratios from our images on the expected blackbody response curve. We paired each CL image with the corresponding IR image that was closest to it in time. The signals were found using IRAF as discussed in Section 2.2.

To find each signal ratio, we divided the CL signal for one image with the signal from the neighboring IR image. We then plotted the ratio for each image pair on the expected blackbody curve to find the corresponding color temperature. A typical plot is shown in Fig. 3.1 for Pillan and plots for the other hotspots are found in Appendix B. The error bars in the plot are $\sim 1\sigma$ and were found using the error analysis outlined in Appendix A. Each data point or ratio value on the curve is comprised of a CL and IR image chosen such that they are the closest images in time and are considered simultaneous.

To find the lava compositions, we considered the highest and lowest color temperatures and associated errors found for each hotspot. We then estimated the lava compositions at each hotspot by comparing the two color temperatures and errors to temperatures of terrestrial lavas of known composition.

3.2 IR Signal Strength

Because of the low IR signal, the validity of many of our temperatures was questionable. The most crucial detector of questionable temperatures was the strength of the IR signal relative to the noise or IR signal error. The IR signal was at the limits of detectability and varied a lot because of uncertainty in the measurement, leading to bad temperature values. For example, low IR signal in some images contributed to an abnormally high temperature value because the background happened to be fluctuating higher at the time the image was taken. This led to a larger background subtraction at that point and thus a smaller IR signal

and higher color temperature. Because of these fluctuations and the errors involved, not all of the temperatures were reliable.

We used a basic signal-to-noise ratio (S/N) analysis to determine which temperature points to keep and which points to remove. We divided the IR signal by the IR signal error to determine the IR S/N for each image and hotspot. This resulted in values ranging from 2.79 down to 0.40, which are very low. Ideally, we would prefer S/N values of 10 or greater, but the quality of the IR images was not sufficient. Given the quality of the IR images and our range of S/N values, we decided on an IR S/N cutoff value of 1.5 or greater. We kept temperatures with an IR S/N value of 1.5 or greater and removed the ones with values smaller than 1.5. This S/N value means that the error is more than half of the signal value, which is not good. Ultimately, this translates into suspect temperatures for even the ones we kept. A summary of this temperature analysis for Pillan, Wayland, and Loki is shown in Tables 3.1, 3.2, and 3.3, respectively. We removed a total of 12 temperature values from Pillan, 6 from Wayland, and 4 from Loki using this analysis.

We also removed temperatures that were not physical such as negative temperatures or extremely high temperatures. These occurred when the IR signal was negative, really small, or non-existant because their was no IR image to pair with the CL image. This removed an additional four temperatures from Pillan, five from Wayland, and two from Loki.

Finally, we removed an additional two temperatures and their corresponding electron fluxes for Loki because they occurred near the beginning and the end of the eclipse. The increased light on the surface of Io as it emerged from behind Jupiter or before it was completely eclipsed caused an anomalous increase in the signal (Fig. 3.2 and Fig. 3.3). This increase made the first and last electron fluxes too high on day364 and unreliable for consideration in our analysis. We previously removed the temperature on day001 corresponding to the elevated signal in Figure 3.3 because it had a low IR S/N. We also removed the electron

Hotspot	T	Error	CL Sig. Flux	Error	IR Sig. Flux	Error	IR S/N
Pillan	K	K	counts/s	counts/s	counts/s	counts/s	
day364	780*	189	19.94	3.54	5.43	2.19	2.48
	1298	337	21.60	3.66	2.16	1.82	1.19
	1085*	280	19.48	3.51	2.83	1.80	1.57
	1761	439	21.27	3.64	1.09	1.53	0.71
	2121	473	19.51	3.41	0.66	1.64	0.40
	1047*	273	18.99	3.46	2.98	1.88	1.58
	1892	459	20.36	3.57	0.89	1.50	0.59
day000	1684	364	23.40	4.15	1.32	1.45	0.91
	1036	288	12.47	3.40	1.99	1.66	1.20
	2097	415	18.34	3.81	0.64	1.49	0.43
	1130*	289	19.02	3.82	2.54	1.58	1.61
day001	1220	312	22.37	3.66	2.55	1.90	1.35
	1802	443	23.78	3.75	1.17	1.63	0.71
	1589	401	22.88	3.72	1.47	1.59	0.93
	1410	352	24.16	3.81	2.02	1.67	1.21
	1023*	255	20.10	3.52	3.30	1.85	1.78
	2008	477	22.77	3.72	0.87	1.49	0.58
day002	934*	216	22.08	3.64	4.32	1.99	2.17

Table 3.1 *Table showing the temperature confidence analysis for Pillan. Only the temperatures selected with a star whose S/N ratio was greater than 1.5 were used in the analysis. Twelve temperatures were not used in the analysis.*

Hotspot	T	Error	CL Sig. Flux	Error	IR Sig. Flux	Error	IR S/N
Wayland	K	K	counts/s	counts/s	counts/s	counts/s	
day364	1695	404	34.69	4.46	1.93	1.74	1.11
	2118	499	32.08	4.31	1.09	1.67	0.65
	1464	357	27.72	4.05	2.13	1.70	1.25
	2048	484	23.91	3.81	0.87	1.49	0.59
day000	1297*	289	28.93	4.47	2.89	1.61	1.79
	1116*	250	26.27	4.30	3.60	1.80	2.00
	1192*	272	25.00	4.20	2.99	1.62	1.85
day001	1751	434	24.83	3.78	1.29	1.64	0.78
	1473	391	16.58	3.24	1.26	1.72	0.73

Table 3.2 *Table showing the temperature confidence analysis for Wayland. Only the temperatures selected with a star whose S/N ratio was greater than 1.5 were used in the analysis. Six temperatures were not used in the analysis.*

Hotspot	T	Error	CL Sig. Flux	Error	IR Sig. Flux	Error	IR S/N
Loki	K	K	counts/s	counts/s	counts/s	counts/s	
day364	1034*	186	16.00	1.54	2.57	0.97	2.65
	1387*	287	20.19	1.65	1.75	0.97	1.80
	1652	397	15.93	1.53	0.94	0.92	1.02
	1306*	300	14.16	1.47	1.40	0.92	1.52
	1541	344	18.29	1.58	1.26	0.87	1.44
	1538	345	18.62	1.61	1.28	0.91	1.42
day001	1692	368	23.67	1.69	1.32	0.91	1.46
	1017*	177	16.55	1.51	2.74	0.98	2.79
	1023*	197	13.77	1.44	2.26	0.92	2.45

Table 3.3 *Table showing the temperature confidence analysis for Loki. Only the temperatures selected with a star whose S/N ratio was greater than 1.5 were used in the analysis. Four temperatures were not used in the analysis.*

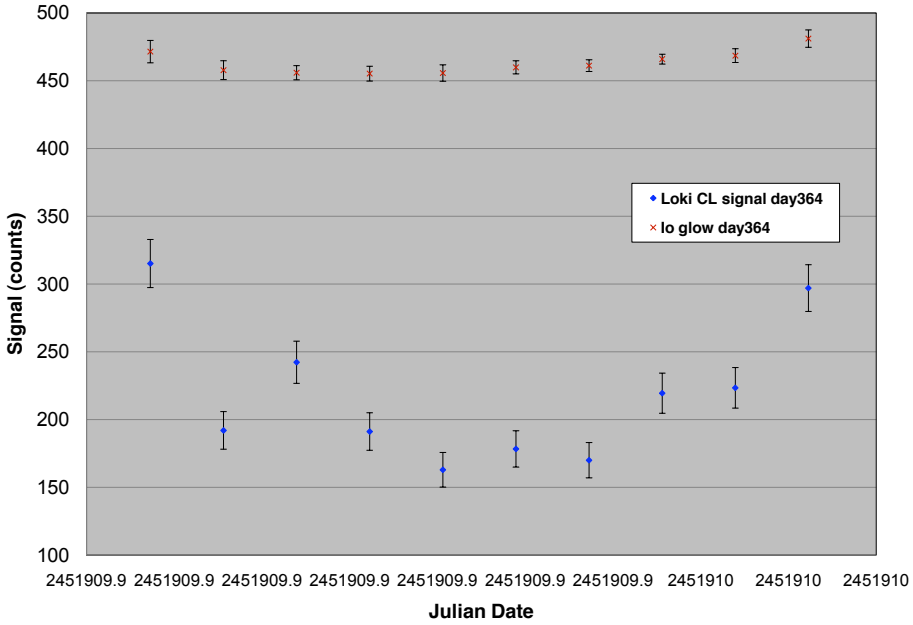

Figure 3.2 *Plot of the Io glow and Loki CL hotspot signal during the eclipse on day364. The first and last points are elevated for both indicating that the Io glow contributes to the hotspot signal. There is extra contribution from the Sun rather than just the signal from the hotspot. Thus, the signal for the first and last observations were not used in the analysis.*

flux for this point because of the elevated signal and Io glow. Similarly, we removed the first electron flux value on day000 for Pillan because it occurred at the beginning of the eclipse.

3.3 Color Temperatures and Lava Compositions

We found very similar color temperatures and consequently lava compositions for all three hotspots. Pillan showed a variation of 350 K from a high of 1130±289 K on day000 to a low of 780±189 K on day364 (see Fig. 3.1 and Table 3.4). These temperatures are consistent with previous values found for Pillan (Davies et al., 2001; McEwen et al., 1998b) and indicate the presence of basaltic lava. Lava at the surface of Io cools rapidly suggesting that these

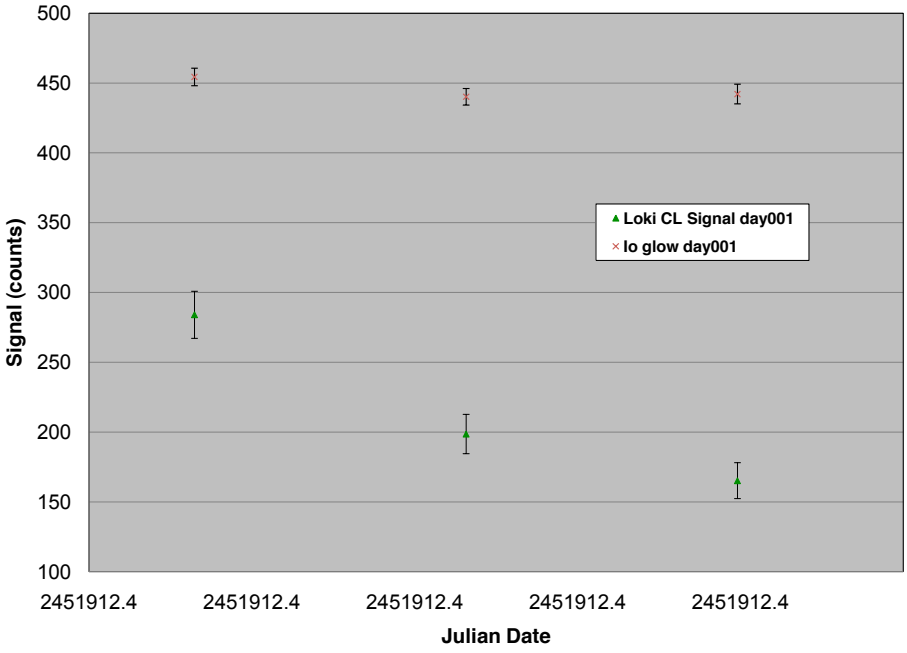

Figure 3.3 *Plot of the Io glow and Loki CL hotspot signal during the eclipse on day001. The first point is elevated for both indicating that the Io glow contributes to the hotspot signal. There is extra contribution from the Sun rather than just the signal from the hotspot. Thus, the signal for the first observation was not used in the analysis.*

temperatures underestimate the eruption temperature by as much as 200 K (Keszthelyi and McEwen, 1997). Even with the addition of 200 K, the composition is still likely basaltic.

Wayland's variation from high to low was 181 K with values of 1297±289 K and 1116±250 K, respectively. These temperatures also indicate the presence of basaltic lava. Wayland had not been previously studied in two-filter observations, so this is the first temperature measurement of this hotspot (Geissler et al., 2004).

We found the highest observed temperatures to date for Loki. As discussed previously in section 1.3 temperatures have been <1000 K and generally around 300-700 K (Davies, 2003; Howell and Lopes, 2007; McEwen et al., 1998a; Rathbun et al., 2002). We found a maximum

Hotspot	High T(K)	Low T(K)	Mean T (K)	Composition
Pillan	1130±289	780±189	962±126	basaltic
Wayland	1297±289	1116±250	1193±91	basaltic
Loki	1387±287	1017±177	1093±179	basaltic

Table 3.4 *The maximum and minimum temperatures for each hotspot with errors as well as the mean and standard deviation. The composition is interpreted from both the high and low temperature values.*

temperature of 1387±287 K and a low temperature of 1017±177 K, with a total range of 370 K. The temperatures suggest basaltic lava composition and are consistent with a well-insulated, cooling lava surface such as a lava lake or thick flows. Higher temperatures have been seen, but rarely (Blaney et al., 1995). A small angle of emission would enable the camera to see deeper into possible cracks on the lava surface and thus see higher temperatures. The emission angles for Loki were low and ranged from $\sim 30.4^o$ to $\sim 12.5^o$. With Cassini observing Loki from almost directly overhead, we are likely seeing down into cracks on the surface and getting higher temperatures than previously seen.

Chapter 4

Variations in Emission

4.1 Finding Variations

In addition to finding color temperatures to infer lava composition, we used the images to track variations in intensity and temperature over time and emission angle for each hotspot. These variations allow us to determine the eruption style since different types of eruptions exhibit characteristic temporal behaviors (Davies et al., 2001).

The determination of the variations and thus eruption styles are twofold. First, the positions of the spacecraft and hotspots are used to find the angle of emission as seen by Cassini. This angle changes throughout the eclipse as Io rotates and the spacecraft moves resulting in a change in emission from the hotspot. The way it changes in relation to what we expect for a flat radiator can be used to determine the geometry of the hotspot and the surrounding area. Second, the temperature and electron flux variations as functions of time and emission angle are found, plotted and used together to determine the eruption style.

4.1.1 Emission Angle

The emission angle was found using the positions of Cassini and the hotspots. It is defined as the angle between a vector normal to the surface of the moon at the position of the hotspot and a vector pointing to Cassini as seen in Fig. 4.1. We used spherical geometry to calculate

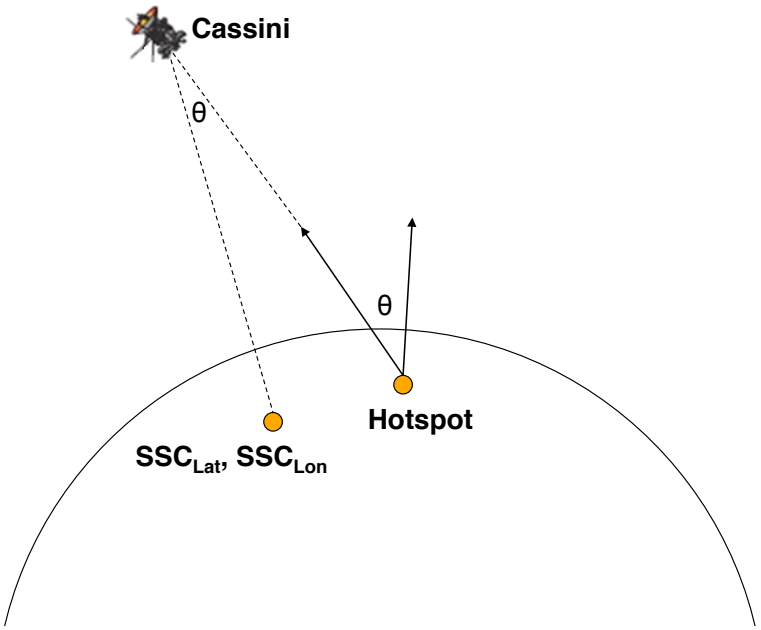

Figure 4.1 *Emission angle, θ, is the angle between a vector normal to the surface and a vector pointing at Cassini from the hotspot. The point directly below Cassini is located at the sub-spacecraft latitude (SSC_{Lat}) and sub-spacecraft longitude (SSC_{Lon})*

the emission angle given the latitude and longitude of the hotspot and the sub-spacecraft latitude (SSC_{lat}) and sub-spacecraft longitude (SSC_{lon}). The SSC_{lat} and SSC_{lon} are defined at the point directly below the spacecraft on the surface of the moon (see Fig. 4.1). The equation for emission angle, θ, is given by:

$$\cos\theta = \cos(90^o - HS_{lat})\cos(90^o - SSC_{lat}) + \sin(90^o - HS_{lat})\sin(90^o - SSC_{lat})\cos(SSC_{lon} - HS_{lon}), \quad (4.1)$$

where HS_{lat} and HS_{lon} are the hotspot latitude and longitude, respectively, and all values are expressed in degrees. The hotspot position is constant, but the sub-spacecraft position changes as Io rotates and Cassini moves.

We found the SSC_{lat} and SSC_{lon} at times specific to our images and calculated the corresponding emission angles. We knew the SSC_{lat} and SSC_{lon} at the start and the end of imaging each day. We also knew the time when imaging began and ended each day. We calculated the time elapsed since the start of imaging to the time our images were taken:

$$t_{elapsed} = t_{image} - t_{start}, \tag{4.2}$$

and used that to find the fraction of total time elapsed since imaging began for each image:

$$t_{fraction} = \frac{t_{elapsed}}{t_{total}}. \tag{4.3}$$

Using the fraction of time elapsed, we found the SSC_{lat} and SSC_{lon} for each image with the following equations:

$$SSC_{lat} = SSC^{o}_{lat} + SSC^{diff}_{lat} t_{fraction}, \tag{4.4}$$

$$SSC_{lon} = SSC^{o}_{lon} + SSC^{diff}_{lon} t_{fraction}, \tag{4.5}$$

where SSC^{o}_{lat} and SSC^{o}_{lon} are the initial sub-spacecraft latitude and longitude, and SSC^{diff}_{lat} and SSC^{diff}_{lon} are the total change in sub-spacecraft latitude and longitude over the eclipse. Finally, we used equation 4.1 and the values for hotspot position and sub-spacecraft position to find the emission angles for our images.

4.1.2 Electron Flux

We found the electron flux values using the CL filter hotspot signal, the integration or image exposure time, and the NAC gain. We then applied a multiplication factor to account for the surface features and rotation of Io to get a corrected flux. First, we divided the CL

signal in units of DN by the integration time and multiplied that by the known gain of 12 electrons/DN (or electrons/count) for the NAC to get the initial measured electron flux in electrons/s for each hotspot.

Second, in an attempt to account for the rotation of Io and any surface features surrounding the hotspots, we multiplied the measured flux by a multiplication factor to get a corrected electron flux. This multiplication factor is defined as

$$m = (1/\cos\theta)^x, \tag{4.6}$$

where θ is the emission angle and x is a factor which linearizes the corrected electron flux. As Io rotates, more or less of the hotspot is visible depending on surface features that may or may not block the feature and whether the hotspot's emission angle is increasing or decreasing. For a flat, constant radiator, we expect the emission to decrease by a factor of $\cos\theta$ or x = 1. A larger or smaller x factor gives us an idea of the geometry of the hotspot and surrounding area. An x factor > 1 indicates a more rapid increase or decrease in electron flux than is expected for a flat radiator and a less rapid increase or decrease for an x factor < 1.

The expectation for the value of the x factor from previous work (Radebaugh et al., 2004; Marchis et al., 2001) is a positive number greater than one. Marchis et al. (2001) suggested there was topography surrounding the hotspot, Pele, which blocked the emission with increasing emission angle. This resulted in a value of 1.3 and thus a greater decrease in emission than expected for a flat radiator (Marchis et al., 2001). Studies of Cassini eclipse data for Pele by Radebaugh et al. (2004) resulted in an x factor of 1.6, indicating an even greater decrease in emission than expected.

We found the x factors by plotting the corrected electron flux as a function of CL filter emission angle starting with an x value of one. We also plotted a linear fit to the corrected flux. Then, we changed the x value until the slope of the linear fit was closest to zero. The

results were inconclusive for Loki, but meaningful results were found for Pillan and Wayland.

Finally, we plotted the electron fluxes as a function of the CL filter emission angle. We also plotted the color temperature versus CL filter emission angle and the temperature and measured electron flux versus time expressed as Julian date. Plots of the mean temperature and mean flux for each day as functions of time show the day to day variations for each hotspot. All of these plots were considered in our determinations of the eruption styles and are discussed in detail in the results, Section 4.2.

4.2 Eruption Styles

We found the eruption styles for the three volcanoes using the plots of electron flux and temperature variations with time and emission angle. With low counts in the IR images, careful consideration of the changes in the electron flux and temperature from one data point to another as well as the relative strength of the IR signal (see Sec. 3.2) was crucial in interpreting the temperature changes. Most of the plots are found in Appendix B with selected plots included in this section.

The temperature as a function of emission angle (Fig. 4.2 and B.1) and as a function of time (Fig. B.2) for Pillan showed no fluctuations within error. A fairly constant output from the volcano would produce this, but with the removal of 12 temperatures from the analysis we lost several data points that may have indicated otherwise.

Pillan's electron flux or total CL filter intensity was constant within error for all three days. It initially appeared to show some significant change with increasing emission angle on day000 (Fig. B.1 and B.2). However, examination of the original image revealed a line of pixels adjacent to the hotspot with low values. They were lower than the midpoint values calculated for the background in their respective rows (see Sec. 2.2). When the background image was subtracted, these low pixels became negative and decreased the final CL signal and

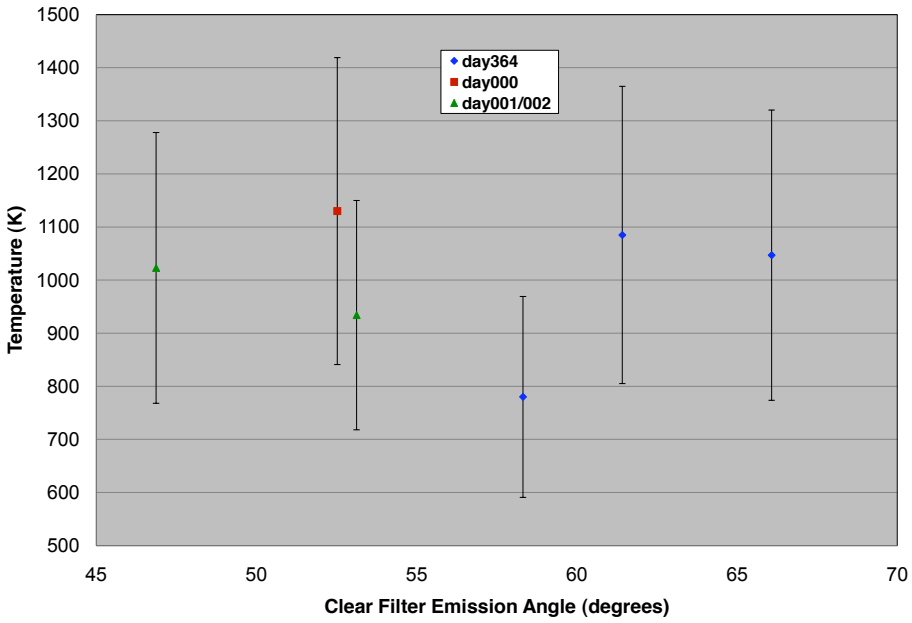

Figure 4.2 *Plot of temperature vs. emission angle for Pillan. With the large errors, there is no variation in the temperature each day. We removed some temperatures that were not considered real (see Sections 2.3 and 3.2).*

consequently the electron flux. Thus the decrease was likely not real and was not considered in our analysis.

Despite being constant within error for all three days (Fig. 4.3), we calculated x values to correct for the expected decreasing emission with decreasing emission angle (see Sec. 4.1.2). We used all of the observations on day364 and day001/002, but we excluded the low point on day000. We found x values of approximately 0.095, 3.13, and 0.36 for day364, day000, and day001/002, respectively. We examined the images for day000 to determine if the large x value was real or a product of instrument error or bad pixels. With the exception of the excluded low point, the images appeared to be okay. The day364 and day001/002 x values indicate a less rapid decrease in emission with increasing emission angle. We expect a decrease in emission by a factor of cos θ or x = 1 as Io rotates. This suggests that day364

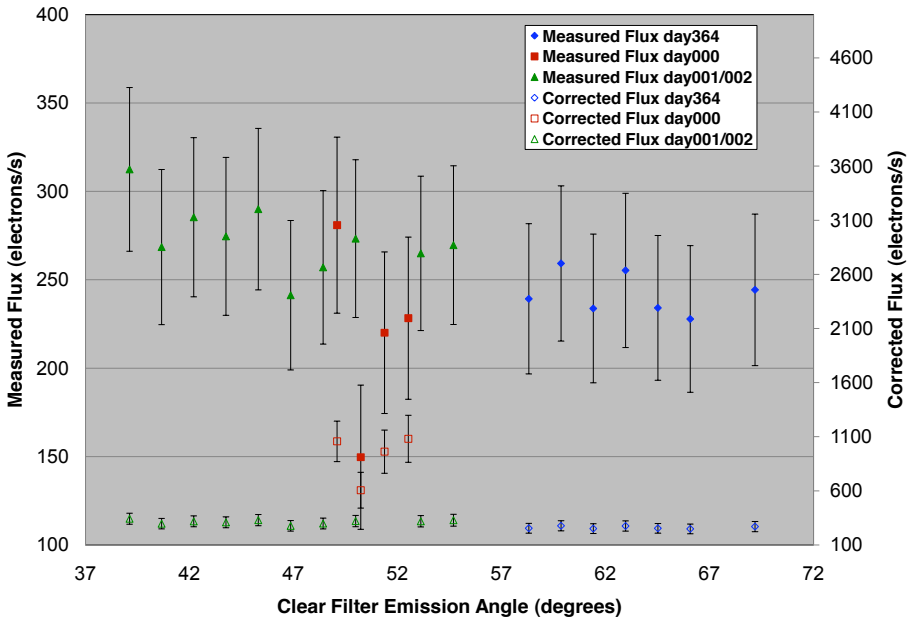

Figure 4.3 *Plot of electron flux versus emission angle for Pillan. The corrected fluxes are plotted on the secondary y-axis. We found x values of 0.095, 3.13, and 0.36 for day364, day000, and day001/002, respectively.* ***Note****: We used all points on day364 and day001/002, but we excluded the low point on day000.*

and day001/002 may have experienced some increased activity on these days to keep the emission from decreasing as expected. The high value for day000 suggests that there may be some topography near the hotspot which blocks the emission and makes it drop more rapidly than expected. However, these x values are not definitive and the large errors in the electron flux values suggest the emission is constant within error.

Mean intensity for Pillan increased on day001/002 after being constant within error for the first two days, indicating an overall increase in volcanic output as seen in the top left plot of Fig. B.7. It showed an increase from 242±12 electrons/s to 273±19 electrons/s over a period of about 42 hours. The increase may also be caused by the lower average emission angle on day001 compared with day000. A lower emission angle allows the spacecraft to see

more of the hotspot and receive increased flux. Nevertheless, this overall increase in emission over the three eclipse observations may indicate increased activity from fountains or newly erupted lava.

Wayland showed the most consistent temperatures. The temperatures were constant in time and with increasing emission angle on day000, the only day for which we had reliable temperature observations (Fig. 4.4, B.3, and B.4). Like Pillan, this indicates a fairly constant output.

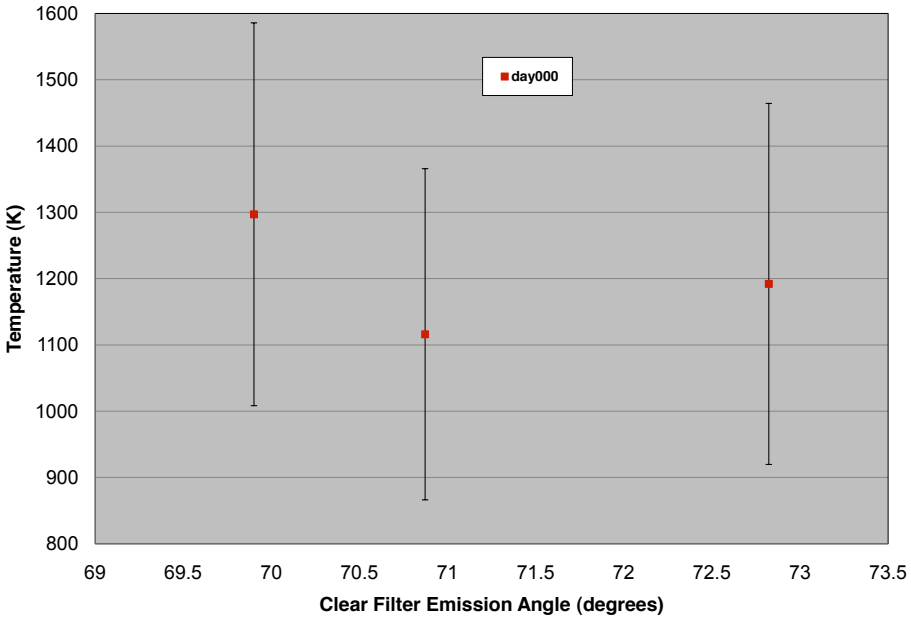

Figure 4.4 *Plot of temperature vs. emission angle for Wayland. With the large errors, there is no variation in the temperature each day. We removed some temperatures that were not considered real (see Sections 2.3 and 3.2).*

Wayland's intensity decreased similarly on all three days (Fig. 4.5). It began at 416±54 electrons/s, 420±58 electrons/s, and 298±45 electrons/s for day364, day000, and day001, respectively. It decreased fairly steadily to 287±46 electrons/s, 256±48 electrons/s, and 118±32 electrons/s in 36 minutes, 26 minutes and 24 seconds, and 48 minutes, respectively.

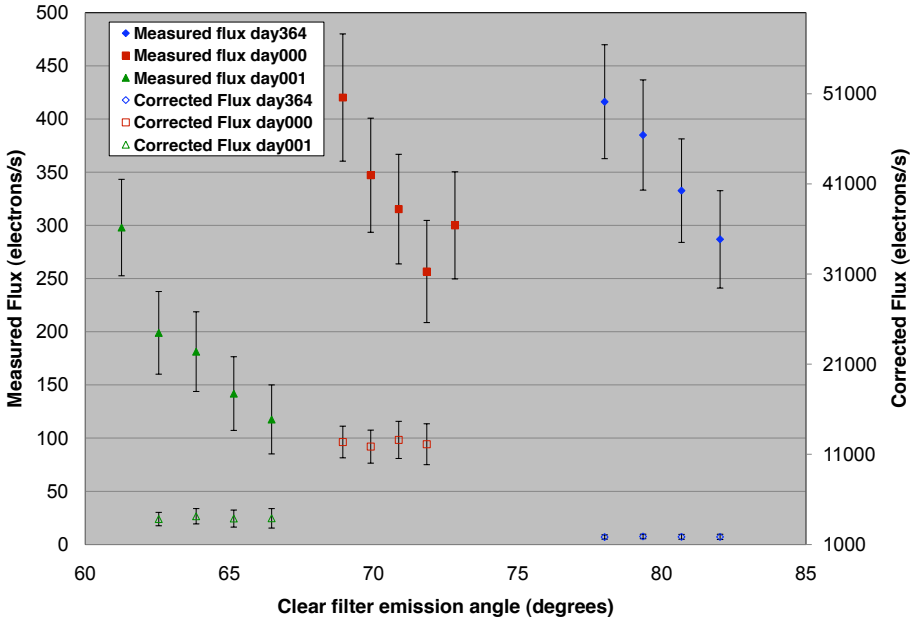

Figure 4.5 *Plot of electron flux versus emission angle for Wayland. The measured flux decreases as the emission angle increases. The corrected fluxes are plotted on the secondary y-axis. We found x values of 0.94, 3.31, and 3.82 for day364, day000, and day001, respectively.* ***Note****: We used all points on day364, the first 4 on day000, and the last 4 on day001 to find the x values.*

Emission angle increased by approximately 4^o over these same time intervals for all three days.

We calculated x values for all three days to see if the decrease in intensity was because of a decrease in emission or a decrease from increasing emission angle. For the calculations, we used the four observations on day364, but we only used the first four observations on day000 and the last four observations on day001 because the other measurements appeared to be errant points. Examination of the original images revealed a line of brighter pixels adjacent to the hotspot in both of the images which contributed to an increased hotspot flux. The increased flux from these lines of pixels may be real, but it is unlikely because none of the

other images on those days showed a similar pattern. We found x values for day364, day000, and day001 of approximately 0.94, 3.31, and 3.82, respectively. These values indicate that the emission is decreasing close to or a little less rapidly than the expected decrease by a factor of cos θ for day364 and decreasing much more rapidly on day000 and day001. Day364 may have some increased activity that keeps the emission from decreasing. The large x values for day000 and day001 suggest some large topographic feature near the hotspot that may be blocking the emission and causing such a large decrease. Galileo SSI images of the area appear to show a depression at Wayland that may explain the topography (Fig. 4.6).

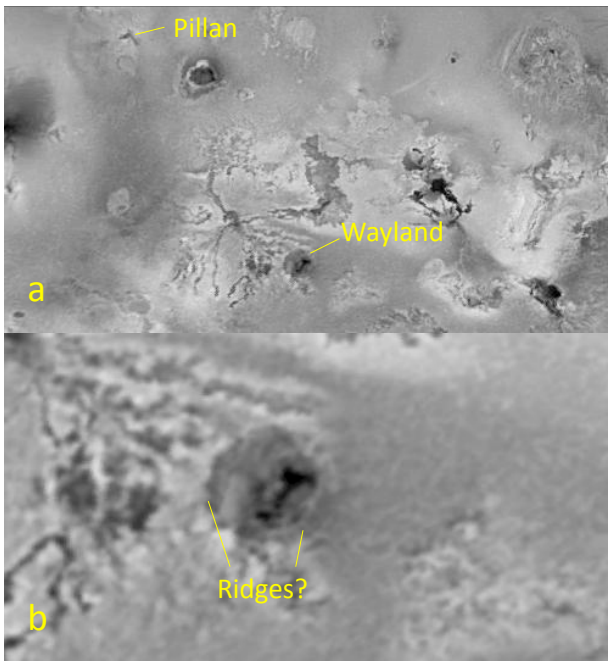

Figure 4.6 *Grayscale Galileo SSI images (USGS Map-a-planet website) showing the region around Wayland and the hotspot itself. Wayland appears to be in a circular depression with ridges around the margins.* ***Note****: Image (a) has a scale of ∼4 km/pixel and image (b) has a scale of ∼1 km/pixel.*

The mean intensity of Wayland also decreased over timescales of tens of hours to several

days (Fig. B.7). It decreased from a mean of 349±57 electrons/s on day364 to 174±70 electrons/s on day001 over a period of around 61 hours. These overall decreases in emission are indicative of a cooling lava flow or crust.

Loki showed no variations in temperature with time or with emission angle for either day (Fig. 4.7, B.5, and B.6). Once again this may indicate a lack of variation in the volcano or

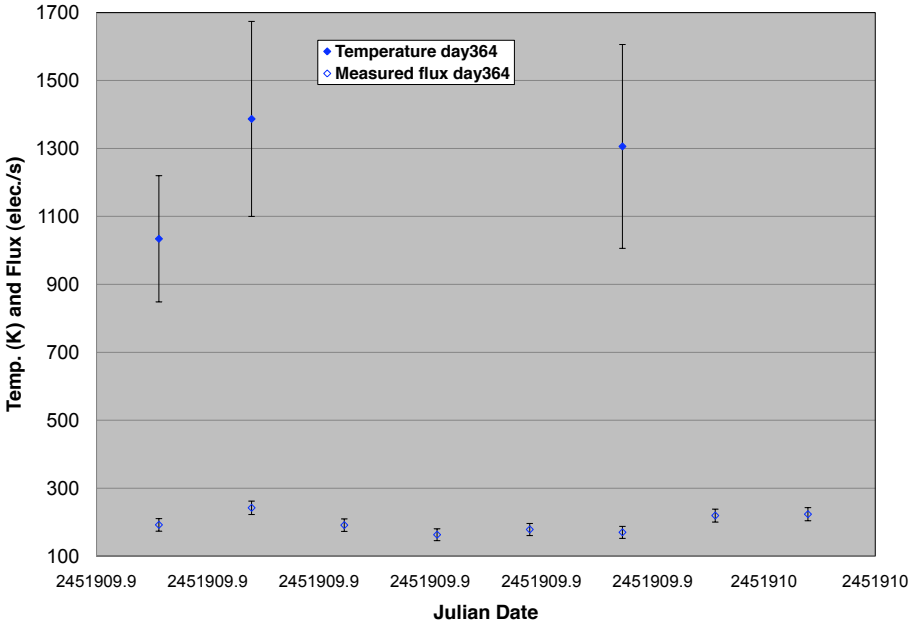

Figure 4.7 *Plot of time variation for Loki on day364. Temperature and measured electron flux are both plotted on the y-axis. Temperature depends on the CL and IR filters, while flux depends only on the CL filter. Five temperature values were not plotted because three had low IR signal-to-noise ratios and were considered unreliable (see Sec. 3.2), one had a negative IR signal, and one didn't have a corresponding IR filter image.*

a lack of sufficient data to really characterize it.

The intensity showed both increases and decreases on day364 and was constant within error on day001. Intensity began day364 at a value of 192±18 electrons/s and an emission angle of 13.9^o (Fig. 4.7). It increased rapidly to a value of 242±20 electrons/s over a period

of 12 minutes and then decreased to a value of 191±18 electrons/s over the same time period. It remained relatively constant within error for the next 36 minutes before rising to a value of 219±19 electrons/s in 12 minutes. These variations are indicative of highly exposed lava eruptions. Given the fact that it is a recurring event on a short timescale, it may be attributed to lava fountains on the surface of an active lava lake (Fig. 4.8). The

Figure 4.8 *Photo of Erta Ale lava lake in the Afar depression of the East African rift zone in Ethiopia. This photo from a 2002 expedition by Alean et al. shows a lava fountain in the center and hot cracks in the cooler, dark crust. There is greater emission from the fountain and also at the central cracks and margins of the lake where the crust breaks up.*

electron flux appears to increase and then decrease systematically with increasing emission angle (Fig. B.5), but calculations of the x values were inconclusive.

The mean intensity on timescales of tens of hours to several days for Loki was constant within error (Fig. B.7). This suggests a fairly constant overall output, indicative of a lava lake.

Unlike the other two hotspots, the change in emission angle didn't correspond to the

change in time for the observations of Loki. The Pillan and Wayland plots for flux as functions of time and emission angle show the same variations. This is not so for Loki. The reason for this is shown in Fig. 4.9. As Io rotated and Cassini moved, Loki rotated into better view of the spacecraft and then out again. The emission angle decreased from 14.6^o to a value of 12.5^o and then back to 14.2^o on day364.

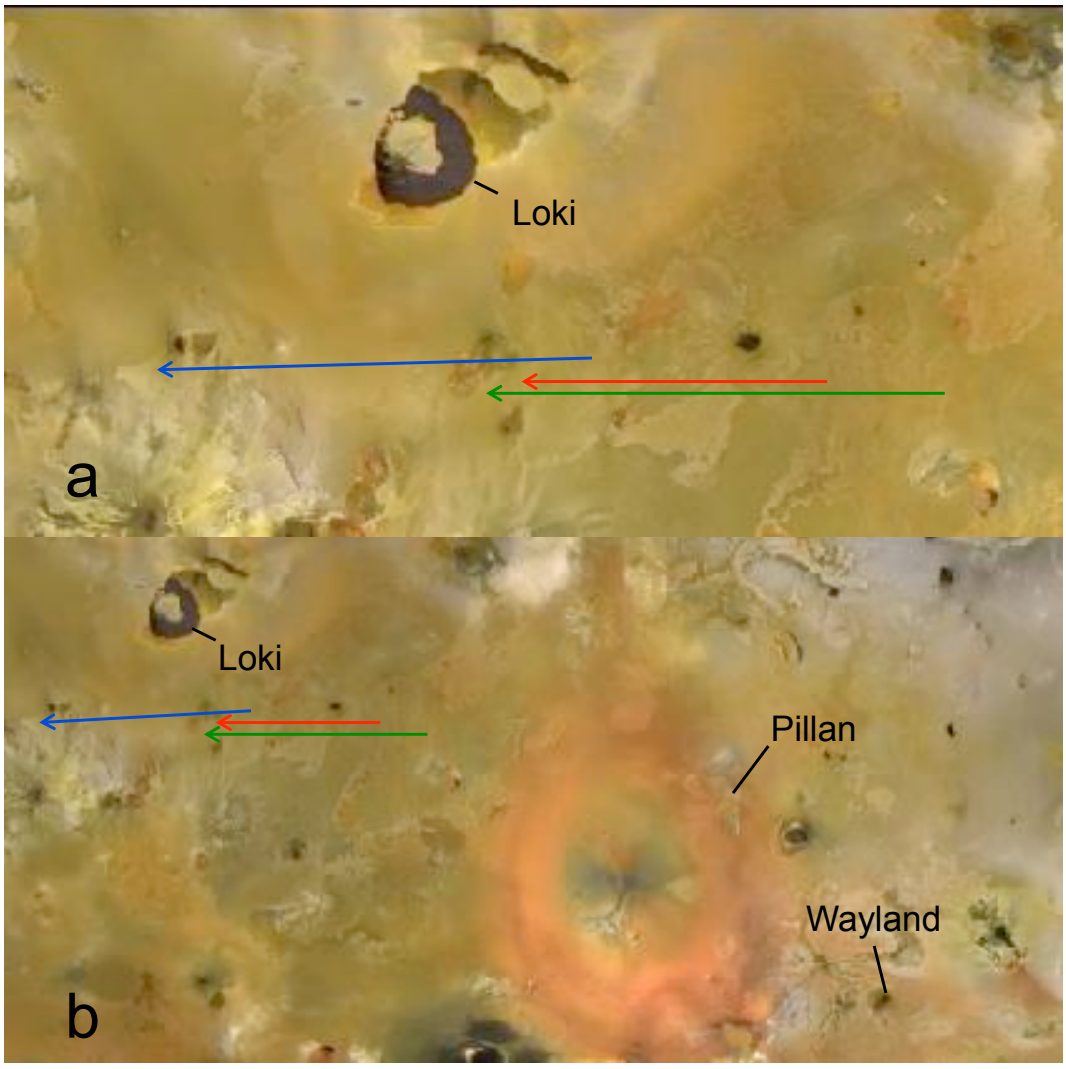

Figure 4.9 *False-color Galileo images (USGS Map-a-planet website) showing the region around our hotspots and the approximate subspacecraft position of Cassini on Io's surface. The colored lines correspond to the three eclipse days and follow the same color scheme seen in all the plots. Pillan and Wayland are below the lines, and as Io rotates and Cassini proceeds from right to left across the surface, the emission angle increases. The emission angle for Loki decreases and then increases as Io rotates and Cassini moves.* ***Note****: The top image has a scale of ∼5 km/pixel and the bottom has a scale of ∼9 km/pixel.*

Chapter 5

Discussion and Conclusions

This analysis of Cassini observations of Io in eclipse by Jupiter during late 2000 and early 2001 provided meaningful results concerning temperatures and eruption styles. We found high and low color temperatures of 1130±289 K and 780±189 K for Pillan, 1297±289 K and 1116±250 K for Wayland, and 1387±287 K and 1017±177 K for Loki. These were all very similar and indicate the presence of basaltic lava at all three. It could be argued that the extreme end of Loki's high temperature indicates ultramafic lava, but it is unlikely. The temperatures with the best IR S/N for Loki are all around 1000 K while the highest temperature has an IR S/N of 1.8 (Table 3.3). A basaltic lava composition with temperatures around 1000 K is more believable and more consistent with previous measurements. The same general trend holds true for Pillan and Wayland. The low temperature of 780±189 K for Pillan corresponds to the highest IR S/N value and the lowest IR S/N value corresponds to the highest Wayland temperature. Many if not all of the temperatures are questionable because of the low IR signal which makes it difficult to definitively say one way or the other, but the compositions are most likely basalt at all three hotspots.

Before the Galileo spacecraft, scientists debated whether the volcanism on Io was sulfur or silicate in origin. It is clear now that the volcanism is dominantly silicate, but the debate now

is whether it is simply basaltic or ultramafic. Temperatures in the ultramafic range have been found before as discussed in section 1.3 (Davies et al., 2001; McEwen et al., 1998b; Radebaugh et al., 2004; Spencer et al., 1997). Three main hypotheses have been proposed for the high temperatures. Ultramafic volcanism is the first and most accepted (Lopes and Williams, 2005; McEwen et al., 1998b). The others are superheated basalt (Kargel et al., 2003; McEwen et al., 1998b) and 'ceramic' volcanism (Kargel et al., 2003). As discussed previously (see Section 1.3), Keszthelyi et al. (2007) believe these temperatures overestimate the actual temperatures by as much as 300 K. Our temperatures aren't conclusive one way or another, but basaltic volcanism is favored.

The eruption styles are more difficult to characterize given our limitations in the IR and lack of high-spatial data that would enable the calculation of areas for the emitting lava. Pillan was particularly difficult to characterize given that none of the daily variations appeared to be real. The overall increase over the three days suggests increased activity on at least the final day of observations. Whether the increased activity was from fountaining, a new lava flow, or cracks on a crust, we don't know. Correction of the electron fluxes for the three days seemed to indicate increased activity on day364 and on day001/002 while the x value for day000 indicated some topography surrounding the hotspot that blocked some of the emission. However, the x values were far from conclusive since the daily variations in electron flux were constant within error. Wayland is probably a cooling lava flow or lava lake at a period of low activity or quiescence given the fairly steady decrease in emission. Analyses of the x values suggest Wayland may be in a depression surrounded by ridges, which is similar to many hotspots on Io. More observations of this volcano are needed to really characterize it. Loki showed the most significant variations over the three days, and the data suggest a lava lake with periods of active overturning and fountains. This is consistent with what has been previously seen at Loki.

Our observations contribute to the overall knowledge of Io's composition and distribution of volcanoes across the surface. Our results are consistent with previous values for the hotspots on Io and with the overall models at present. While they don't shift the paradigm from mafic to ultramafic lava composition or suggest a radical change to the accepted models, our results give us more clues as to what is happening on the surface of this moon. The viability of the Cassini data to measure the temperature of these faint hotspots using a color temperature technique is questionable because of the low IR signal. As a result, the temperatures are all questionable. Clearly, more research is needed to fully understand Io and its violent history, and in particular these three hotspots.

Bibliography

Alean, J., Carniel, R., & Fulle, M., "Stromboli Online - Volcanoes of the World," Available: http://www.swisseduc.ch/stromboli/

"IRAF Project Home Page," Available: http://iraf.noao.edu/

Anderson, J., "USGS Isis: About Isis," Available: http://isis.astrogeology.usgs.gov/AboutIsis/index.html

Binder, A.P. and Cruikshank, D.P., 1964. Evidence for an atmosphere on Io. Icarus **3**, 299-305.

Blaney, D.L., Johnson, T.V., Matson, D.L., Veeder, G.J., 1995. Volcanic eruptions on Io: Heat flow, resurfacing, and lava composition. Icarus **113**, 220-225.

Carr, M.H., 1986. Silicate volcanism on Io. J. Geophys. Res., **91**, 3521-3532.

Casadevall, T., Rose, W., Gerlach, T., Greenland, L.P., Ewert, J., Wunderman, R., Symonds, R., 1983. Gas emissions and the eruptions of Mount St. Helens through 1982. Science, **221**, 1383-1385.

Christiansen, E.H. and Hamblin, W.K., 1995. Exploring the Planets. Prentice Hall.

Cassini Imaging Science Team, "ISS: Cassini's High-Resolution Imaging Science Camera System," Available: http://ciclops.org/iss/iss.php

Davies, A.G., 1996. Io's volcanism: Thermo-physical models of silicate lava compared with observations of thermal emission. Icarus **124**, 45-61.

Davies, A.G., McEwen, A.S., Lopes-Gautier, R.M.C., Keszthelyi, L., Carlson, R.W., Smythe, W.D., 1997. Temperature and area constraints of the South Volund volcano on Io from the NIMS and SSI instruments during the Galileo G1 orbit. Geophys. Res. Lett. **24**(20), 2447-2450.

Davies, A.G., Keszthelyi, L.P., Williams, D.A., Phillips, C.B., McEwen, A.S., Lopes, R.M.C., Smythe, W.D., Kamp, L.W., Soderblom, L.A., Carlson, R.W., 2001. Thermal signature, eruption style, and eruption evolution at Pele and Pillan on Io. J. Geophys. Res., **106**, 33079-33103.

Davies, A.G., 2003. Temperature, age and crust thickness distributions of Loki patera on Io from Galileo NIMS data: implications for resurfacing mechanism. Geophys. Res. Lett. **30**, 2133.

Davies, A.G., Keszthelyi, L.P., Wilson, L., 2006. Estimation of maximum effusion rate for the Pillan 1997 eruption on Io: implications for massive basaltic flow emplacement on Earth and Mars. Lunar and Planetary Science Conference XXXVII, Abstract 1155.

Davies, A.G., 2007. Volcanism on Io: A Comparison with Earth. New York: Cambridge University Press.

de Pater, I., Marchis, F., Macintosh, B.A., Roe, H.G., Le Mignant, D., Graham, J.R., Davies, A.G., 2004. Keck AO observations of Io in and out of eclipse. Icarus **169**, 250-263.

European Space Agency, "ESA-Cassini-Huygens," Available: http://www.esa.int/SPECIALS/Cassini-Huygens/

Fanale, F.P., Brown, R.H., Cruikshank, D.P., Clake, R.N., 1979. Significance of absorption features in Io's IR reflectance spectrum. Nature **280**, 761-763.

Francis, P.W. and Rothery, D.A., 1987. Using the Landsat Thematic Mapper to detect and monitor active volcanoes: an example from the Lascar volcano, northern Chile. Geology **15**, 614-617.

Geissler, P.E., McEwen, A.S., Keszthelyi, L., Lopes-Gautier, R., Granahan, J., Simonelli, D.P., 1999. Global color variations on Io. Icarus **140**, 265-282.

Geissler, P.E., McEwen, A., Porco, C., Strobel, D., Saur, J., Ajello, J., West, R., 2004. Cassini observations of Io's visible aurorae. Icarus **172**, 127-140.

Grossman, L., 1972. Condensation in the primitive solar nebula. Geochimica et Cosmochimica Acta **36**, 597-619.

Howell, R.R., 1997. Thermal emission from lava flows on Io. Icarus **127**, 394-407.

Howell, R.R. and Lopes, R.M.C., 2007. The nature of the volcanic activity at Loki: Insights from Galileo NIMS and PPR data. Icarus **186**, 448-461.

Johnson, T.V., Veeder, G.J., Matson, D.L., Brown, R.H., Nelson, R.M., Morrison, D., 1988. Io: evidence for silicate volcanism in 1986. Science **242**, 1280-1283.

Kargel, J.S., Delmelle, P., Nash, D.B., 1999. Volcanogenic sulfur on Earth and Io: composition and spectroscopy. Icarus **142**, 249-280.

Kargel, J., Carlson, R., Davies, A., Fegley Jr., B., Gillespie, A., Greeley, R., Howell, R., Jessup, K.L., Kamp, L., Keszthelyi, L., Lopes, R., MacIntyre, T., Marchis, F., McEwen, A., Millazo, M., Perry, J., Radebaugh, J., Schaefer, L., Schmerr, N., Smythe, W., Spencer,

J., Williams, D., Zhang, J., Zolotov, M., 2003. Extreme volcanism on Io: Latest insights at the end of Galileo era. EOS Trans. AGU **84**, 313-318.

Keszthelyi, L. and McEwen, A.S., 1997. Thermal models for basaltic volcanism on Io. Geophys. Res. Lett. **24**, 2463-2466.

Keszthelyi, L., McEwen, A.S., Phillips, C.B., Milazzo, M., Geissler, P., Turtle, E.P., Radebaugh, J., Williams, D.A., Simonelli, D.P., Breneman, H.H., Klaasen, K.P., Levanas, G., Denk, T., 2001. Imaging of volcanic activity on Jupiter's moon Io by Galileo during the Galileo Europa Mission and the Galileo Millennium Mission. J. Geophys. Res. **106**, 33025-33052.

Keszthelyi, L., Jaeger, W.L., Turtle, E.P., Milazzo, M., Radebaugh, J., 2004. A post-Galileo view of Io's interior. Icarus **169**, 271-286.

Keszthelyi, L., Jaeger, W., Milazzo, M., Radebaugh, J., Davies, A.G., Mitchell, K.L., 2007. New estimates for Io eruption temperatures: Implications for the interior. Icarus **192**, 491-502.

Kieffer, S.W., 1982. Dynamics and thermodynamics of volcanic eruptions: implications for the plumes on Io. In Satellites of Jupiter. Tucson: University of Arizona Press.

Laver, C., de Pater, I., Marchis, F., 2007. Tvashtar awakening detected in April 2006 with OSIRIS at the W.M. Keck Observatory. Icarus **191**, 749-754.

Lopes-Gautier, R., Davies, A.G., Carlson, R., Smythe, W., Kamp, L., Soderblom, L., Leader, F.E., Mehlman, R., 1997. Hot spots on Io: Initial results from Galileo's near infrared mapping spectrometer. Geophys. Res. Lett. **24**(20), 2439-2442.

Lopes-Gautier, R., McEwen, A.S., Smythe, W.S., Geissler, P.E., Kamp, L., Davies, A.G., Spencer, J.R., Keszthelyi, L., Carlson, R., Leader, F.E., Mehlman, R., Soderblom, L.,

Galileo NIMS and SSI teams, 1999. Active volcanism on Io: Global distribution and variations in activity. Icarus **140**, 243-264.

Lopes, R., Kamp, L.W., Smythe, W.D., Mouginis-Mark, P., Kargel, J., Radebaugh, J., Turtle, E.P., Perry, J., Williams, D.A., Carlson, R.W., Doute, S., Galileo NIMS and SSI teams, 2004. Lava lakes on Io: observations of Io's volcanic activity from Galileo during the 2001 fly-bys. Icarus **169**, 140-174.

Lopes, R.M.C. and Williams, D.A., 2005. Io after Galileo. Rep. Prog. Phys., **68**, 303-340.

Marchis, F., Prange, R., Fusco, T., 2001. A survey of Io's volcanism by adaptive optics observations in the 3.8μm thermal band (1996-1999). J. Geophys. Res. **106**, 33141-33159.

Marchis, F., de Pater, I., Davies, A.G., Roe, H.G., Fusco, T., Le Mignant, D., Descamps, P., Macintosh, B.A., Prange, R., 2002. High-resolution Keck adaptive optics imaging of violent volcanic activity on Io. Icarus **160**, 124-131.

Marchis, F., Le Mignant, D., Chaffee, F.H., Davies, A.G., Kwok, S.H., Prange, R., de Pater, I., Amico, P., Campbell, R., Fusco, T., Goodrich, R.W., Conrad, A., 2005. Keck AO survey of Io global volcanic activity between 2 and 5μm. Icarus **176**, 96-122.

Matson, D.L., Blaney, D.L., Johnson, T.V., Veeder, G.J., Davies, A.G., 1998. Io and the early Earth. Lunar and Planetary Science Conference XXIX, Abstract 1650.

McEwen, A.S., Keszthelyi, L., Geissler, P., Simonelli, D.P., Carr, M.H., Johnson, T.V., Klaasen, K.P., Breneman, H.H., Jones, T.J., Kaufman, J.M., Magee, K.P., Senske, D.A., Belton, M.J.S., Schubert, G., 1998a. Active volcanism on Io as seen by Galileo SSI. Icarus **135**, 181-219.

McEwen, A.S., Keszthelyi, L., Spencer, J.R., Schubert, G., Matson, D.L., Lopes-Gautier, R., Klaasen, K.P., Johnson, T.V., Head, J.W., Geissler, P., Fagents, S., Davies, A.G.,

Carr, M.H., Breneman, H.H., Belton, M.J.S., 1998b. High-temperature silicate volcanism on Jupiter's moon Io. Science **281**, 87-90.

Milazzo, M.P., Keszthelyi, L., Radebaugh, J., Davies, A.G., Turtle, E.P., Geissler, P., Klaasen, K.P., Rathbun, J.A., McEwen, A.S., 2005. Volcanic activity at Tvashtar Catena, Io. Icarus **179**, 235-251.

Morabito, L.A., Synnott, S.P., Kupferman, P.N., Collins, S.A., 1979. Discovery of currently active extraterrestrial volcanism. Science **204**, 972.

Morrison, D., Cruikshank, D.P., Murphy, R.E., 1972. Temperatures of Titan and the Galilean satellites at 20 microns. Astrophys. J. **173**, L143-146.

Oppenheimer, C.M.M. and Rothery, D.A., 1991. Infrared monitoring of volcanoes by satellite. J. of the Geological Soc. **148**, 563-569.

Peale, S.J., Cassen, P., Reynolds, R.T., 1979. Melting of Io by tidal dissipation. Science **203**, 892-894.

Pearl, J., Hanel, R., Kunde, V., Maguire, W., Fox, K., Gupta, S., Ponnamperuma, C., Raulin, F., 1979. Identification of gaseous SO_2 and new upper limits for other gases. Nature **280**, 755-758.

NASA Jet Propulsion Laboratory, Photojournal: NASA's Image Access Home Page, Available: http://photojournal.jpl.nasa.gov/

Porco, C.C., West, R.A., McEwen, A., Del Genio, A.D., Ingersoll, A.P., Thomas, P., Squyres, S., Dones, L., Murray, C.D., Johnson, T.V., Burns, J.A., Brahic, A., Neukum, G., Veverka, J., Barbara, J.M., Denk, T., Evans, M., Ferrier, J.J., Geissler, P., Helfenstein, P., Roatsch, T., Throop, H., Tiscareno, M., Vasavada, A.R., 2003. Cassini imaging of Jupiter's atmosphere, satellites, and rings. Science **299**, 1541-1547.

Porco, C.C., West, R.A., Squyres, S., McEwen, A., Thomas, P., Murray, C.D., Delgenio, A., Ingersoll, A.P., Johnson, T.V., Neukum, G., Veverka, J., Dones, L., Brahic, A., Burns, J.A., Haemmerle, V., Knowles, B., Dawson, D., Roatsch, T., Beurle, K., Owen, W., 2004. Cassini imaging science: instrument characteristics and anticipated scientific investigations at Saturn. Space Science Reviews **115**, 363-497.

Radebaugh, J., Keszthelyi, L., McEwen, A.S., Turtle, E.P., Jaeger, W., Milazzo, M., 2001. Paterae on Io: a new type of volcanic caldera? J. Geophys. Res. **106**(E12), 33005-33020.

Radebaugh, J., McEwen, A.S., Milazzo, M.P., Keszthelyi, L.P., Davies, A.G., Turtle, E.P., Dawson, D.D., 2004. Observations and temperatures of Io's Pele patera from Cassini and Galileo spacecraft images. Icarus **169**, 65-79.

Rathbun, J.A., Spencer, J.R., Davies, A.G., Howell, R.R., Wilson, L., 2002. Loki, Io: a periodic volcano. Geophys. Res. Letters **29**, doi: 10.1029/2002GL014747.

Rathbun, J.A., Spencer, J.R., Tamppari, L.K., Martin, T.Z., Barnard, L., Travis, L.D., 2004. Mapping of Io's thermal radiation by the Galileo photopolarimeter-radiometer (PPR) instrument. Icarus **169**, 127-139.

Rathbun, J.A. and Spencer, J.R., 2006. Loki, Io: New ground-based observations and a model describing the change from periodic overturn. Geophys. Res. Letters **33**, 17201.

Rothery, D.A., Francis, P.W., Wood, C.A., 1988. Volcano monitoring using short wavelength infrared data from satellites. J. Geophys. Res. **93**, 7993-8008.

Spencer, J.R., Stansberry, J.A., Dumas, C., Vakil, D., Pregler, R., Hicks, M., Hege, K., 1997. A history of high-temperature Io volcanism: February 1995 to May 1997. Geophys. Res. Letters **24**, 2451.

Spencer, J.R., Jessup, K.L., McGrath, M.A., Ballester, G.E., Yelle, R., 2000. Discovery of gaseous S_2 in Io's Pele plume. Science **288**, 1208.

Spencer, J.R., Stern, S.A., Cheng, A.F., Weaver, H.A., Reuter, D.C., Retherford, K., Lunsford, A., Moore, J.M., Abramov, O., Lopes, R.M.C., Perry, J.E., Kamp, L., Showalter, M., Jessup, K.L., Marchis, F., Schenk, P.M., Dumas, C., 2007. Io volcanism seen by New Horizons: A major eruption of the Tvashtar volcano. Science **318**, 240-243.

Stephens, D.C., 2010a. Getval.pl [Computer program]. Provo,UT:Brigham Young University.

Stephens, D.C., 2010b. Rep26t.f [Computer program]. Provo,UT:Brigham Young University.

Stephens, D.C., 2010c. Temphist.f [Computer program]. Provo,UT:Brigham Young University.

USGS Astrogeology, USGS Astrogeology: Map-a-planet. Available: http://www.mapaplanet.org/

Veeder, G.J., Matson, D., Johnson, T., Blaney, D., Goguen, J., 1994. Io's heat flow from infrared radiometry: 1983-1993. J. Geophys. Res. **99**, 17095-17162.

Vlaar, N.J., van Keken, P.E., van den Berg, A.P., 1994. Cooling of the Earth in the Archaean: consequences of pressure-release melting in a hotter mantle. Earth and Planet. Sci. Letters **121**, 1-18.

Wahr, J., 1995. "Earth Tides", Global Earth Physics, A Handbook of Physical Constants, AGU Reference Shelf 1, 40-46.

Wamsteker W., Kroes, R.L., Fountain, J.A., 1974. On the surface composition of Io. Icarus **10**, 17.

Williams, D.A., Davies, A.G., Keszthelyi, L.P., Greeley, R., 2001a. The summer 1997 eruption at Pillan patera on Io: implications for ultrabasic lava flow emplacement. J. Geophys. Res. **106**(E12), 33105-33120.

Williams, D.A., Greeley, R., Lopes, R.M.C., Davies, A.G., 2001b. Evaluation of sulfur flow emplacement on Io from Galileo data and numerical modeling. J. Geophys. Res. **106**(E12), 33161-33174.

Williams, D.A., Radebaugh, J., Keszthelyi, L.P., McEwen, A.S., Lopes, R.M.C., Doute, S., Greeley, R., 2002. Geologic mapping of the Chaac-Camaxtli region of Io from Galileo imaging data. J. Geophys. Res. **107**(E9), 5068.

Wilson, L. and Head, J.W., 1983. A comparison of volcanic eruption processes on Earth, Moon, Mars, Io and Venus. Nature **302**, 663-669.

Wilson, L. and Head, J.W., 2001. Lava fountains from the 1999 Tvashtar Catena fissure eruption on Io: implications for dike emplacement mechanisms, eruption rates, and crustal structure. J. Geophys. Res. **106**, 32997-33004.

Wilson, L. and Head, J.W., 2003. Deep generation of magmatic gas on the Moon and implications of pyroclastic eruptions. Geophys. Res. Letters, **30**(12), 1605.

Witteborn F.C., Bregman, J.D., Pollack, J.B., 1979. Io, an intense brightening near 5 micrometers. Science **203**, 643-646.

Wood, J.S., 2003. "Tidal Heating - Io: Jupiter's Volcanic Moon," Available: http://www.planetaryexploration.net/jupiter/io/tidal_heating.html

Appendix A

Error Analysis

The error analysis was not a trivial task and required the use of traditional error propagation as well as a Monte Carlo technique to find the temperature errors. The following sections describe the complete error analyses.

A.1 Signal Errors

We computed the signal errors using traditional error propagation techniques and an equation to account for both the error introduced by the source or hotspot and the error in the background. The signal error equation was

$$\sigma^2_{signal} = \sigma^2_{source} + n\sigma^2_{background}, \tag{A.1}$$

where n is the number of pixels in the aperture used to find the signal, which in this case was 7.343. The source error was computed using Poisson statistics such that

$$\sigma_{source} = \sqrt{N}, \tag{A.2}$$

where N is the number of counts from the source or the signal. The background error was calculated from the average standard deviation of the pixels in all of the rows in the image,

σ_{pixel}, giving

$$\sigma_{background} = \sigma_{pixel}. \tag{A.3}$$

We found the standard deviation of the pixels in each of the 1024 rows in each image using *gstatistics* in IRAF and averaged them to find σ_{pixel}.

A.2 Monte Carlo Temperature Errors

We used a Monte Carlo simulation to find the errors in the temperatures. The program *temphist.f* (Stephens, 2010c) uses the CL and IR signals and associated errors to find a possible range of temperatures and the standard deviation. It does this by taking the first CL and IR signals from an input file and assuming a gaussian error distribution. It calculates new CL and IR signal values, finds the CL/IR signal ratio, and calculates a new temperature. The program runs this process a million times to get a gaussian distribution of a million temperature values. It finds the mean temperature value from this distribution and the 1-sigma deviation and returns them as the final temperature and error. The process is repeated for each pair of CL and IR signals in the input file, and the results are written to an output file. In our analysis, we used our previously calculated temperature values and the errors given by *temphist.f*.

A.3 Electron Flux Errors

We calculated the electron flux errors using the signal errors as described in Section A.1. The measured electron fluxes were given by

$$F_m = S_{Clear}G, \tag{A.4}$$

where S_{Clear} is the CL filter hotspot signal divided by the exposure time and G is the gain of 12 electrons/DN. The related errors were found using

$$\sigma_{F_m} = G\sigma_{S_{Clear}}. \tag{A.5}$$

We used the calculated errors for the plus and minus of the error bars as seen in Fig. 4.5.

Appendix B

Plots

All of the plots used in the analysis are found here. The essential plots used in the analyses of the hotspots are included first. Pillan plots are shown first followed by Wayland and Loki. Any other plots are included in the last section.

B.1 Essential Plots

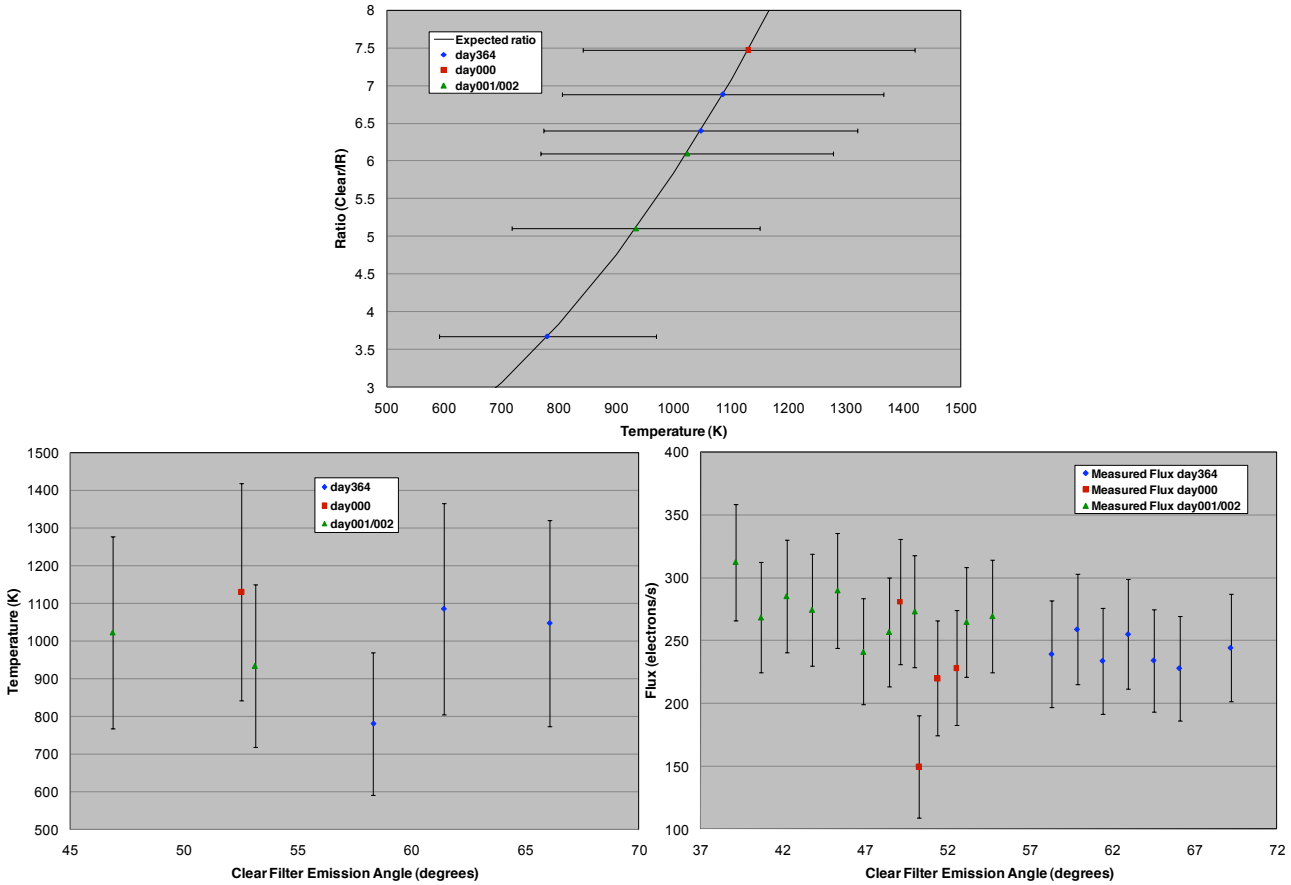

Figure B.1 *Plots for Pillan used in the analysis. The maximum and minimum temperatures in the top plot were used to infer a basaltic lava composition. The other two plots were used to help find the eruption style. The low flux value on day000 was found to be incorrect and was not used in the analysis.*

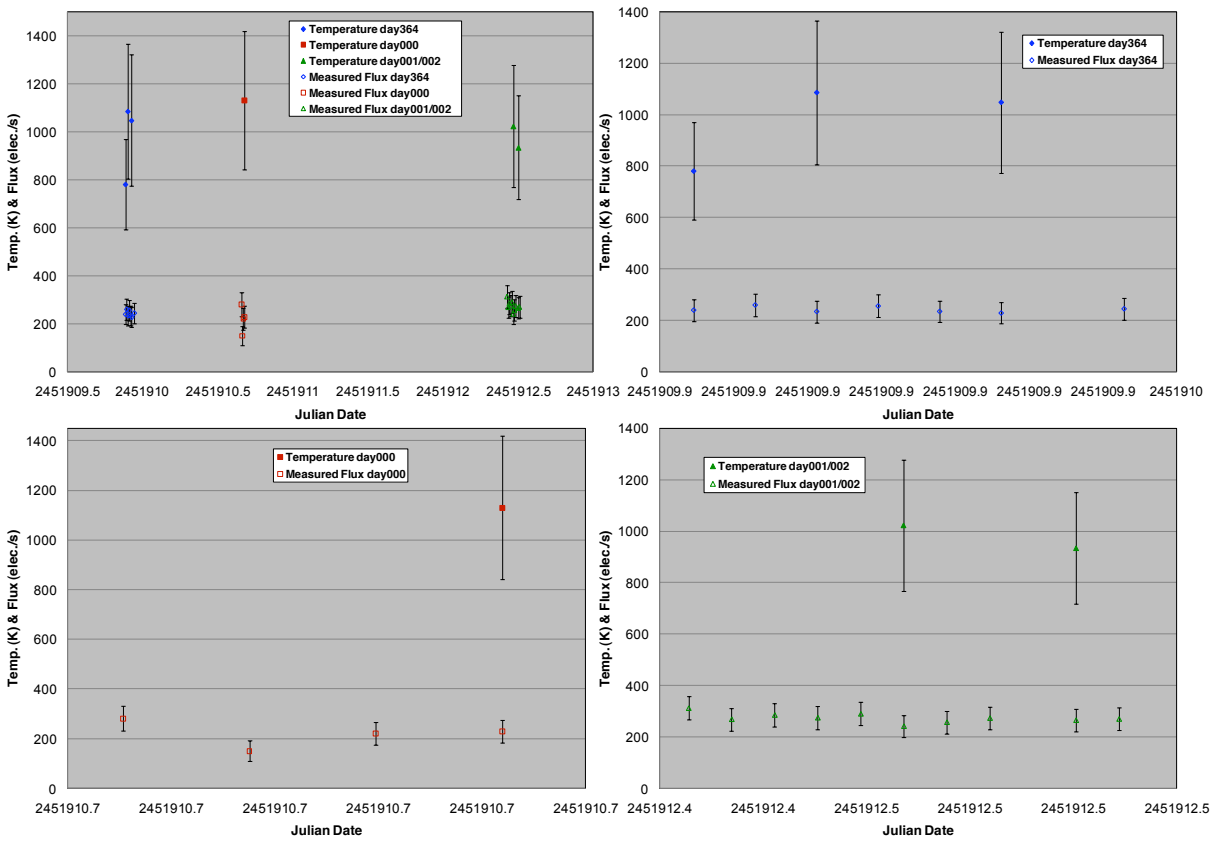

Figure B.2 *Time plots for Pillan used in the analysis. All plots show the temperature and flux on the y-axis with time expressed as Julian date on the x-axis. The fluxes are constant within error and so are the temperatures when the bad data point on day000 is removed. It was found to be low because of a line of low pixel values next to the hotspot.*

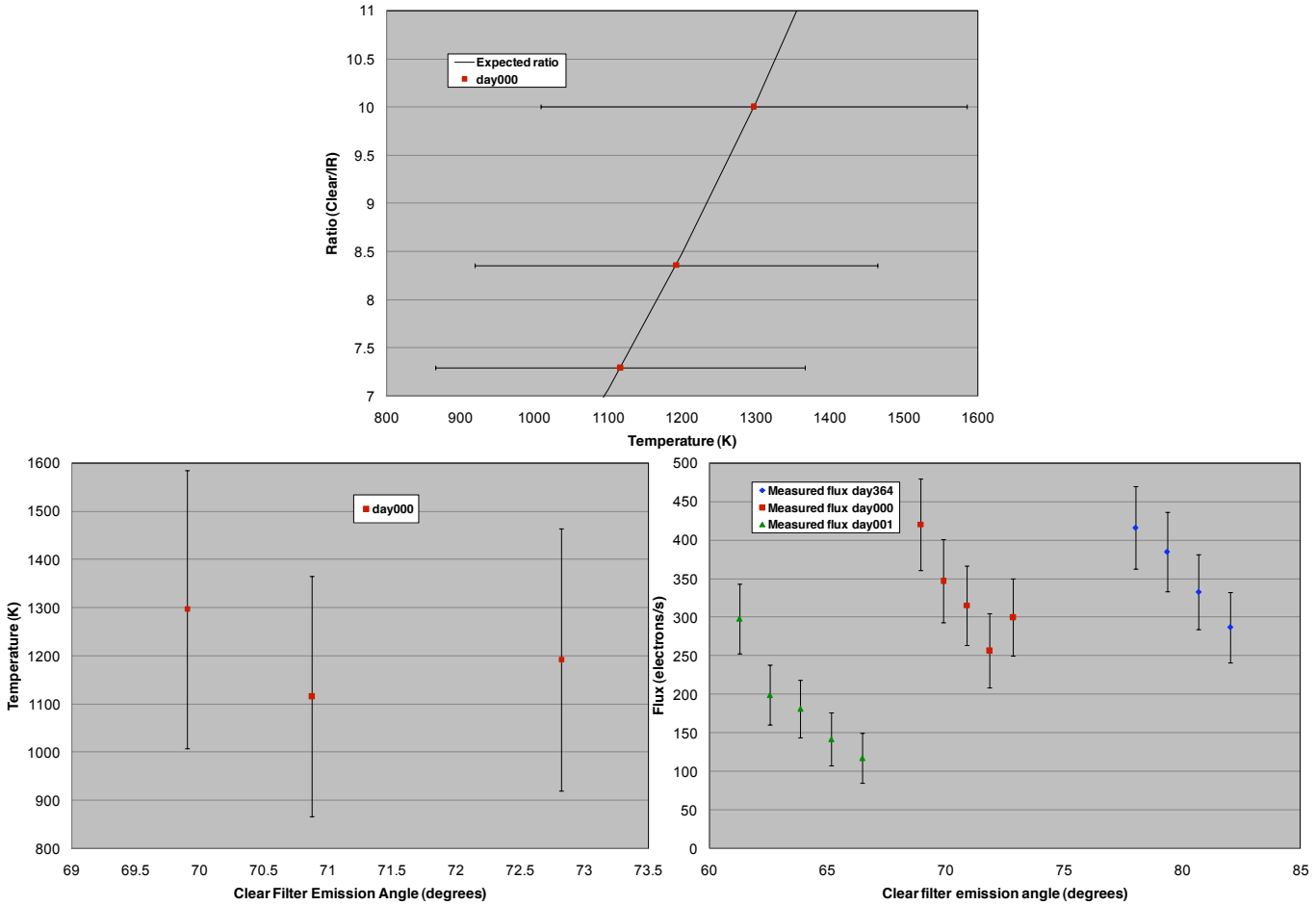

Figure B.3 *Plots for Wayland used in the analysis. The maximum and minimum temperatures in the top plot were used to infer a basaltic lava composition. The other two plots were used to help find the eruption style.*

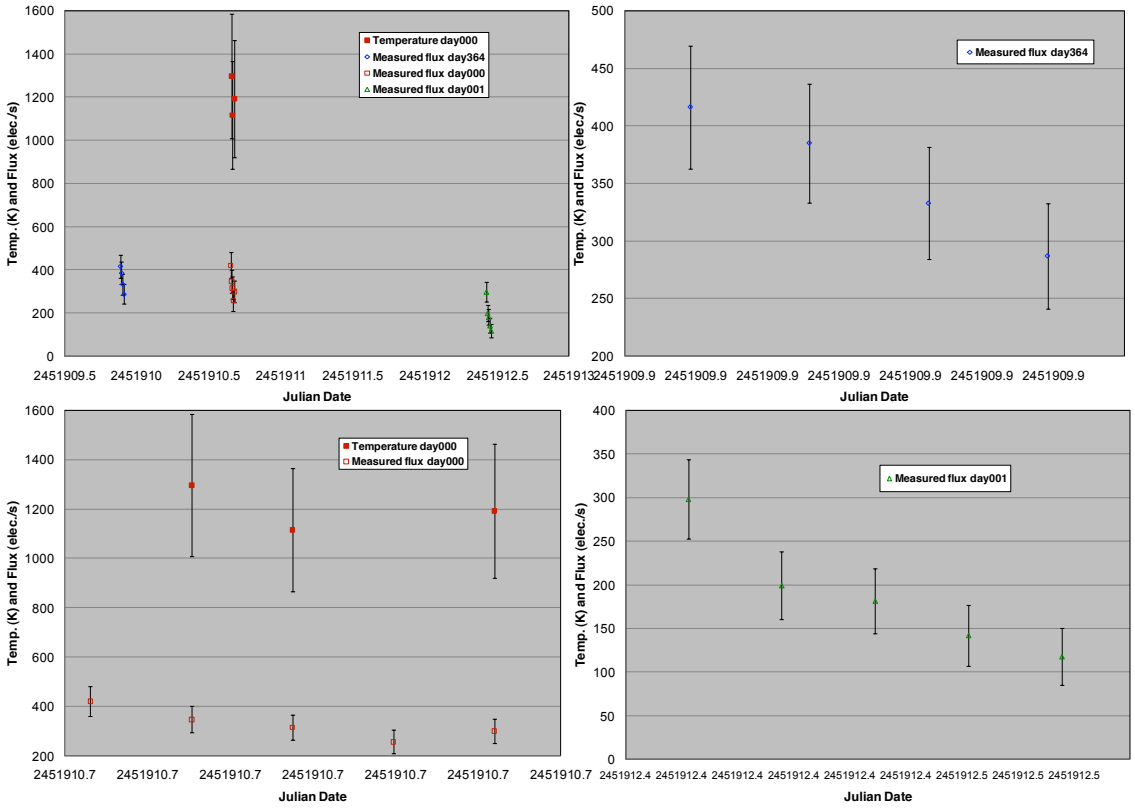

Figure B.4 *Time plots for Wayland used in the analysis. All plots show the temperature and flux on the y-axis with time expressed as Julian date on the x-axis. Temperature is constant within error for each day, but the fluxes show some variation. Day364 and day001 show only the measured fluxes because none of the temperature values were real for those days.*

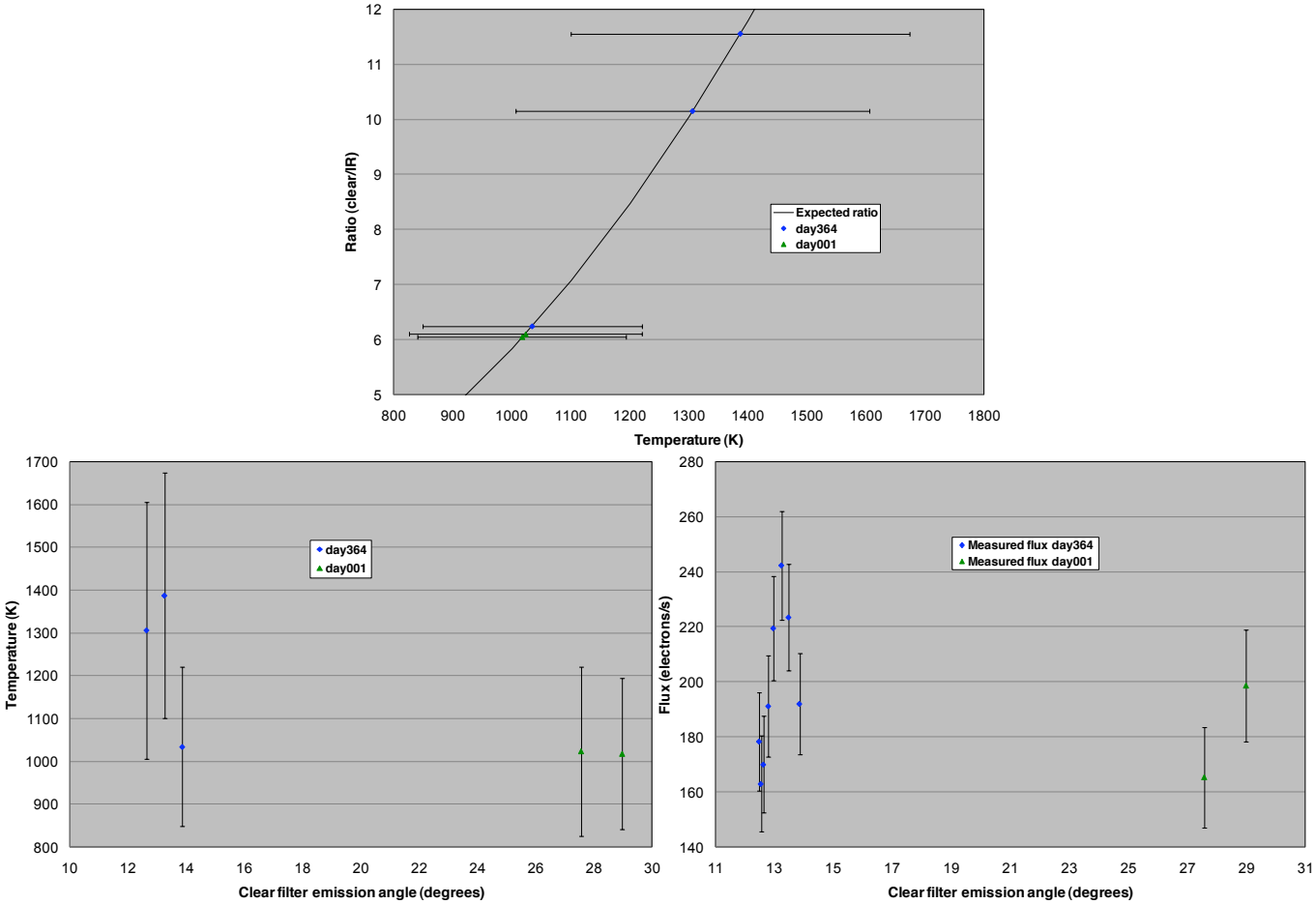

Figure B.5 *Plots for Loki used in the analysis. The maximum and minimum temperatures in the top plot were used to infer a basaltic lava composition. The other two plots were used to help find the eruption style.*

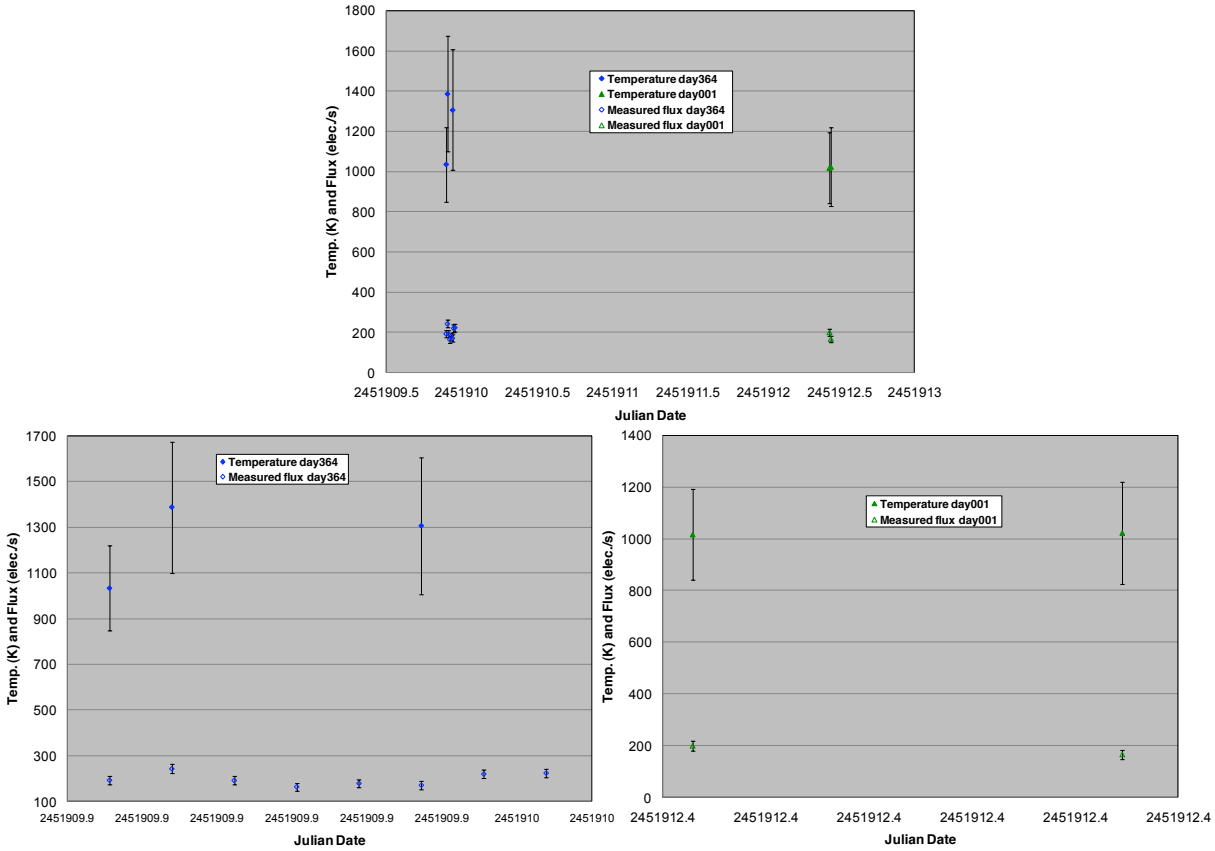

Figure B.6 *Time plots for Loki used in the analysis. All plots show the temperature and flux on the y-axis with time expressed as Julian date on the x-axis. The fluxes show some variation on day364.*

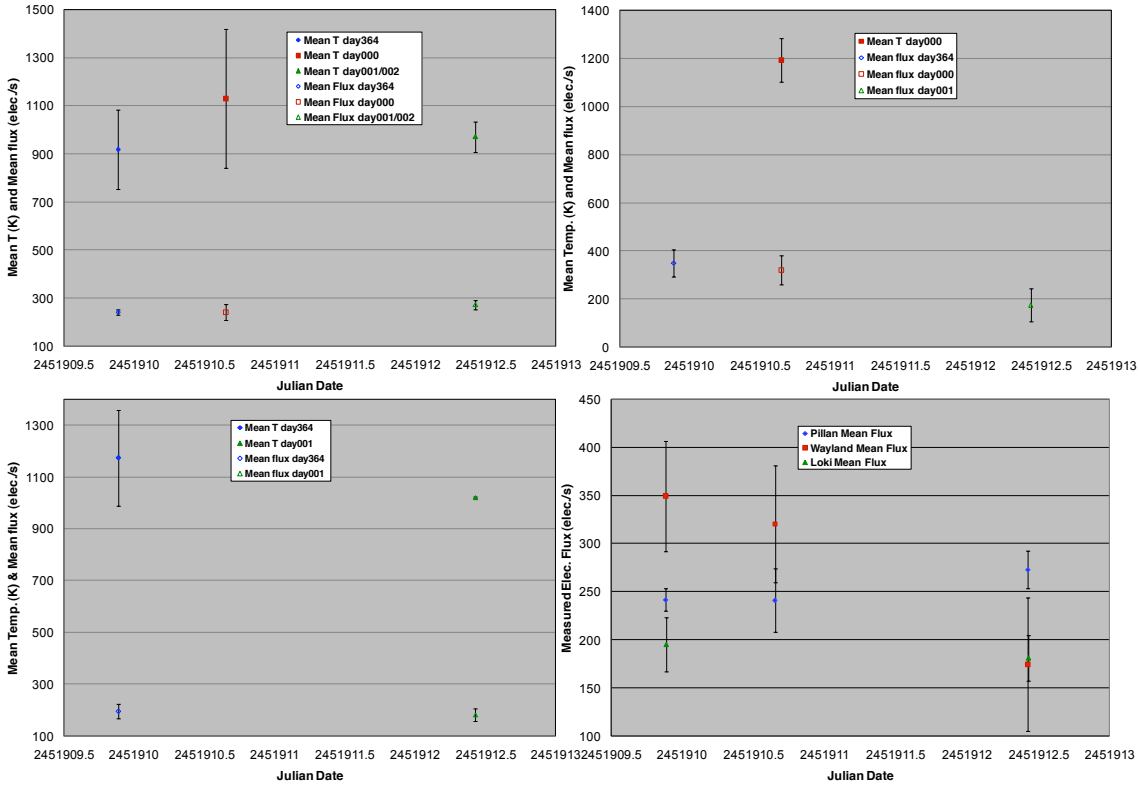

Figure B.7 *Plots showing the day to day variations with time. The mean temperatures were found for each day and plotted at the first time each day. The top left shows Pillan. The top right is Wayland, and the bottom left is Loki. The bottom right shows the mean fluxes each day for all three hotspots on the same plot. They show different variations in flux when compared to one another which rules out the possibility of a systematic error in the data acquisition.*

B.2 Other Plots

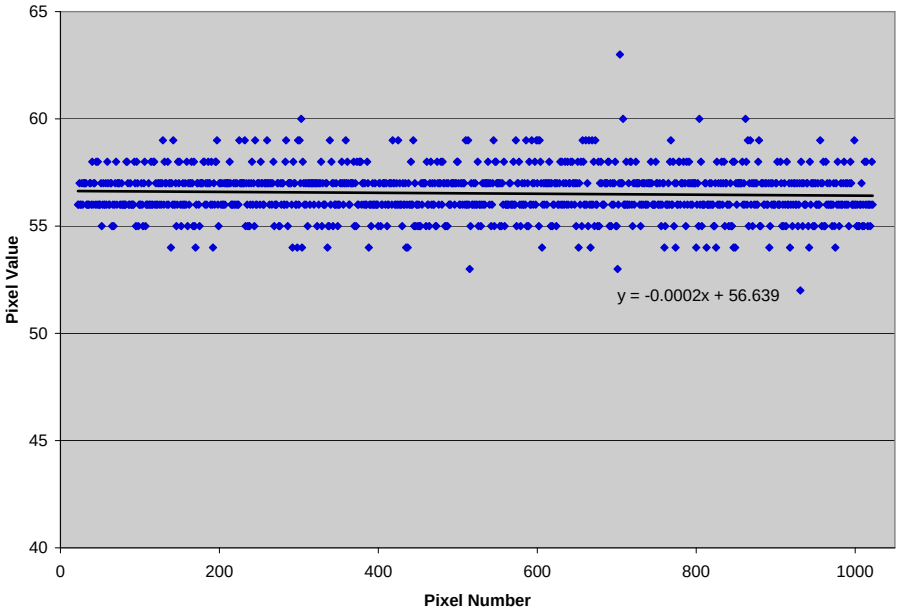

Figure B.8 *A plot of the pixel values down a single line in a typical image. The equation represents a linear fit to the data and indicates a slope of essentially zero as expected. This confirms that the image hum is purely vertical.*

Appendix C

IRAF Packages and Parameters

The following section outlines the IRAF packages and parameters used in the image analysis. The primary IRAF program used to find the flux or signal from each of the hotspots was *phot*, and the user-defined parameters are seen in Figure C.1. The other figures in this section (Fig. C.2, C.3, C.4, & C.5) are the parameter files that must be set in order to run *phot*. The *phot* program is designed to identify stars in a CCD image using the *centerpars* and *datapars* parameters, calculate a background value using parameters outlined in *fitskypars*, subtract that background and find the flux or signal from that star using the parameters outlined in *photpars* and *phot*.

We used a similar technique to find the signal from our hotspots using *phot*. However, we simplified the process because our hotspots were faint and because of the manner in which we processed the images prior to finding the fluxes. For example, we didn't use *fitskypars* to find the background because we had already subtracted it out (see Section 2.2). We also used the x-y coordinate files found previously to specify the hotspot positions rather than using *centerpars* and *datapars* to find the hotspots. We initially tried using *centerpars* and *datapars* to identify the hotspots, but they always jumped to Pele. The other hotspots were too faint.

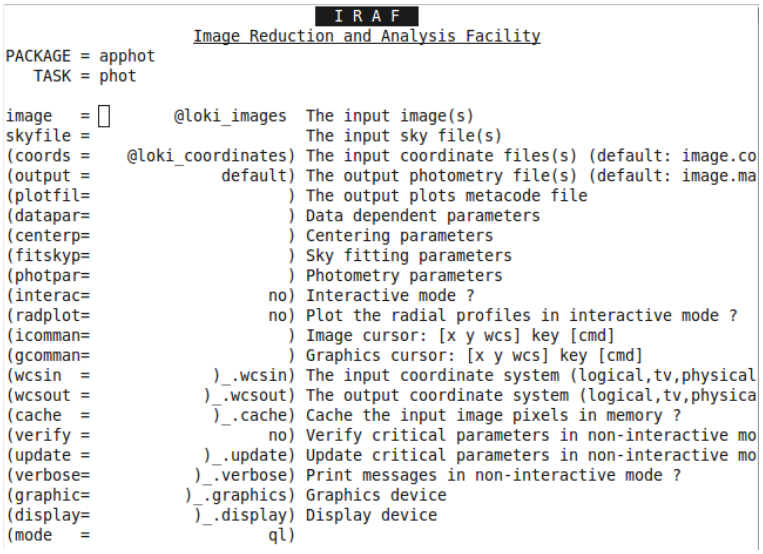

Figure C.1 *The parameters used to process the images and find the flux or signal from the hotspots. The list of images and coordinate files are the important parameters that changed from one hotspot to the next. Phot is able to take a list of images and coordinate files and process them in succession.*

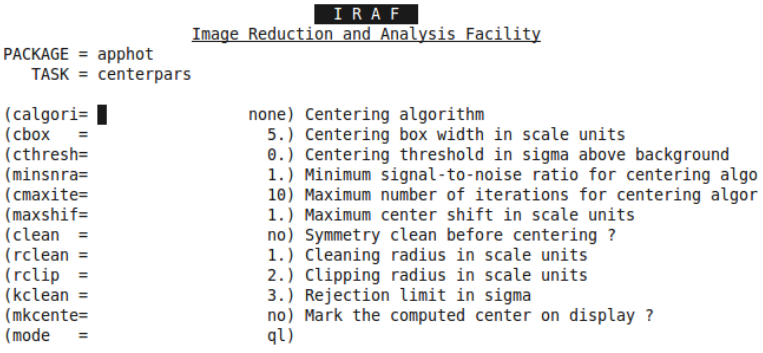

Figure C.2 *The parameters used to find and center the aperture on a star or hotspot. We specified a centering algorithm of none because we used the x-y coordinate files to identify and center our aperture. The other parameters were not used.*

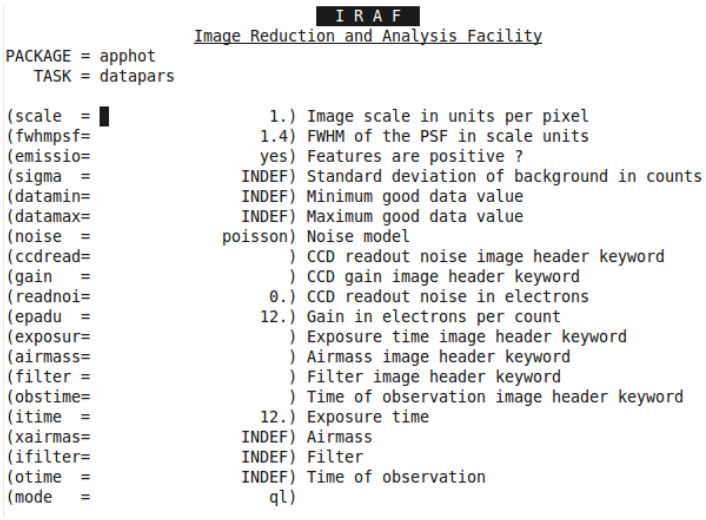

Figure C.3 *The parameters normally used to aid in identifying the stars or hotspots and to identify the specifics of the data. The fwhmpsf parameter aids in finding the star, but we didn't use it. We set the epadu parameter or gain of the camera at 12 electrons/count for all hotspots and changed the itime or exposure time accordingly.*

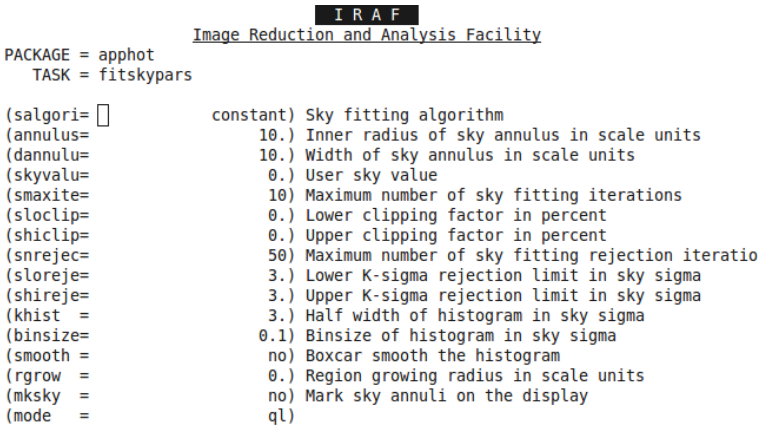

Figure C.4 *The parameters normally used to calculate a background or sky value around a star. We removed the background contribution before processing so the sky fitting algorithm was set to constant. We then set the skyvalu parameter to zero.*

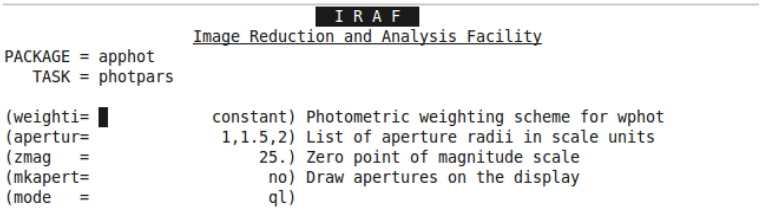

Figure C.5 *The parameters used to specify an aperture size around the star or hotspot. The aperture is circular and is used to calculate the flux or signal from the hotspot. We specified aperture sizes of 1, 1.5 and 2 to get a better understanding of how the flux changed with the different sizes. We ultimately used 1.5 for our calculations.*

Index